Max-Planck-Institut für Meteorologie

REPORT No. 162

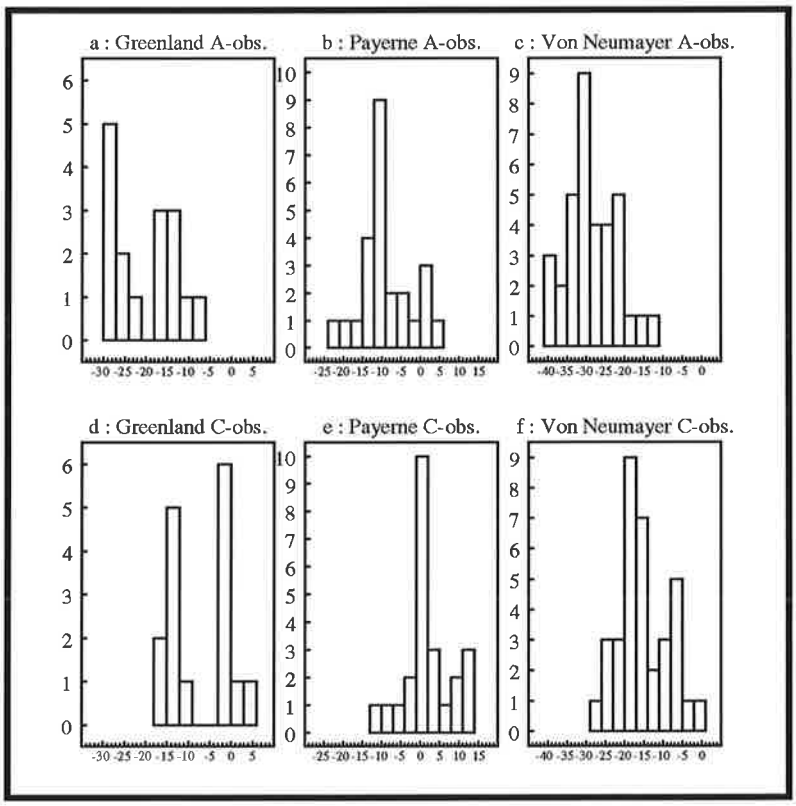

THE WATER VAPOUR CONTINUUM AND ITS REPRESENTATION IN ECHAM4

by

MARCO GIORGETTA • MARTIN WILD

HAMBURG, May 1995

AUTHORS:

Marco Giorgetta — Max-Planck-Institut für Meteorologie
Hamburg, Germany

Martin Wild — Swiss Federal Institute of Technology (ETH)
Zurich, Switzerland

MAX-PLANCK-INSTITUT
FÜR METEOROLOGIE
BUNDESSTRASSE 55
D-20146 HAMBURG
F.R. GERMANY

Tel.: +49 - (0)40 - 411 73 - 0
Telefax: +49 - (0)40 - 411 73 - 298
E-Mail: <name>@dkrz.d400.de

ISSN 0937 – 1060

The Water Vapour Continuum and its representation in ECHAM4

Marco Giorgetta [1] and Martin Wild [2]

[1] Max-Planck-Institute for Meteorology, Hamburg, Germany
[2] Swiss Federal Institute of Technology, Zurich, Switzerland

1 Motivation

The physics of the ECHAM4 general circulation model includes the Morcrette radiation scheme (Morcrette 1984) to compute cooling and heating rates in the free atmosphere and fluxes at the surface. The analysis of the longwave radiation scheme revealed the special role of water vapour among the IR-absorbing and emitting gases in the atmosphere. This is obvious by the fact that water vapour absorption is computed in two terms, i.e. the line term and the continuum term, while absorption rates for all other gases need only the line term. Curiosity for the reason of this distinction lead to the study of the corresponding literature and showed finally a way to improve the performance of the water vapour absorption within this model.

The subsequently presented modifications increase the longwave downward fluxes at the surface in cold and/or dry places and help to bring model results in correspondence with observations.

The following chapters lead from general properties of gaseous absorption to spectral properties of water vapour, water vapour absorption in the atmospheric window region, the definition of the continuum, and to the hypothetical explanations of the continuum. The succeeding chapters cover the continuum parameterization in ECHAM4, the applied modifications, the validation and finally an estimation of the impact on the ECHAM4 climate.

2 The nature of the problem

The absorption and emission of radiation in a gas are inherently quantum mechanical processes. The existence of discrete energy levels of a molecule is a manifestation of the quantum character of systems on the atomic scale. The ground state is the only stable state while any excited molecule lowers its internal energy by a transition to the ground state or another lower state after some time, even if it is unperturbed. The generally transient character of an excited molecular state is bound to an indefiniteness of the energy of the state as it is expressed in Heisenberg's uncertainty relationship. The energy of a photon emitted during a transition between two definite quantum states is therefore undetermined as well, and the transitional energy is statistically distributed around the central energy bound to the two states.

Molecular transitions are either spontaneous decays or happen during an interaction with the radiation field and/or collisions with other molecules. Spontaneous decay times follow a Poisson distribution (1) and hence the distribution of photon energies of a particular transition, the so-called line shape, follows a Lorentz profile (2) of a given half width α centred at the main frequency ν_0 belonging to the undergone transition.

$$p(t) = \frac{1}{\tau} \cdot \exp\left(-\frac{t}{\tau}\right) \tag{1}$$

$$f_L(\nu - \nu_0) = \frac{\alpha}{\pi\left[(\nu - \nu_0)^2 + \alpha^2\right]} \tag{2}$$

$$\alpha = \frac{1}{2\pi\tau} \tag{3}$$

The half width α for spontaneous decay and its mean life time τ are related constants (3) specific for each transition. However transitions in a gas are mostly triggered during collisions or by the radiation field before spontaneous decays occur. The relative motion of the molecules induces also a Doppler effect, allowing more intense absorption farther away from the line centre. This implies that line shapes and line widths of transitions occurring in a gas are no longer constants, but depend on the macroscopic parameters like composition, pressure and temperature which describe the state of the gas. Line broadening by collisions dominates under tropospheric conditions, because of the relatively high pressure and the short mean time between collisions, and is referred to as pressure broadening. Doppler line broadening depends on the temperature and the molecular weight but not on pressure. It must be taken into consideration when the pressure is less than 10 hPa and the pressure broadening is minor. An accurate computation of line shapes therefore requires the knowledge of the state of the gas and of the collisional processes.

Pressure broadening in the mixed gas like the atmosphere is very complex because of the manifold of collisions: binary collisions and (rare) collisions involving three or more molecules, collisions between molecules of the same species and collisions between foreign molecules, collisions with only a weak interaction and short duration and others with a strong interaction and long duration. Due to the complexity of this problem it is inevitable to find useful assumptions and simplifications in the theoretical determination of line shapes.

When Lorentz developed his line shape theory (Lorentz 1906), he assumed an infinitely short duration of collisions, weak interactions and uniform velocity of all molecules in the gas. The first assumption is the so-called impact approximation. The resulting distribution of time between collisions is again a Poisson distribution (1), but τ is now the mean time between collisions, and the line shape, named after Lorentz, is the same as for spontaneous decay (2). This line shape was used extensively in radiation models and often served as a basis for less simplified line shape theories, as for instance the Voigt line shape which includes the Doppler effect (Dicke 1953).

The applicability of approximations has to be tested in computations of radiative transfer based on the derived theoretical line shape and must be verified against laboratory measurements. Such comparisons showed the ability of many independent models to compute the absorption of thermal radiation to a fairly high degree of accuracy for atmospheric absorbers like carbon dioxide, but not for water vapour (Kiehl and Ramanathan 1983).

The following paragraphs compile observations, theoretical considerations and modelling problems related to the special behaviour of water vapour absorption.

3 Water vapour absorption

The following chapter compiles characteristics of the water vapour molecule taken from Goody and Yung (1989, p. 198 ff).

3.1 Spectroscopic properties

Water vapour, carbon dioxide and ozone are the main absorbers and emitters of thermal radiation in the earth's atmosphere. Water vapour plays a special role not only because of its high variability in time and space but also because of its many absorption lines. The water vapour molecule is an asymmetric top with the oxygen atom in the middle, and it has a large permanent electric dipole momentum of $6.16 \cdot 10^{-30}$ Cm and strong rotation lines (CO_2: no permanent dipole moment, rotation bands not permitted; O_3: $1.77 \cdot 10^{-30}$ Cm). The rotation lines occur in widespread line arrays because of the three greatly different but nevertheless small moments of inertia of the molecule. Further the three vibrational fundamentals of water vapour have relative ratios of approximately $\nu_1:\nu_2:\nu_3=2:1:2$, allowing complex interactions between vibrational modes. Therefore the spectrum of water vapour is by far the most complex among the important absorbers in the atmosphere and there is no spectral region in the solar and thermal spectrum without absorption by this molecule. The main activity of water vapour occurs in several spectroscopic band:

- the rotation band in 0-1000 cm^{-1}
- the 6.3μm vibration-rotation band in 900-2400 cm^{-1}
- the 2.7μm group of vibration-rotation bands in 2800-4400 cm^{-1}
- six near-infrared line groups in 4500-11,000 cm^{-1}
- weak visible bands in 11,000-18,000 cm^{-1}

The first three bands are depicted in figure 1 (after Clough et al., 1980) that shows a theoretically derived absorption spectrum for pure water vapour under normel ambient conditions in the wavenumber interval 0 - 5000 cm^{-1}. In this report the focus is set on the absorption in the window between the rotation band and the 6.3μm vibration-rotation band. This interval contains no strong absorption lines but it is nevertheless contributing substantially to the water vapour absorption in the lower atmosphere, since this interval covers the maximum of the blackbody radiation at typical atmospheric temperatures.

3.2 The water vapour continuum

The special role of absorption in the atmospheric window was already recognized by Elsasser in 1942. He found that the absorption of infrared radiation in the window regions, i.e. spectral intervals without any strong lines of any absorber, depended on the humidity. This and later measurements (McCoy et al. 1969, Burch and Gryvnak 1980, Burch 1981, Burch 1985, Burch and Alt 1984) in the atmosphere or in the laboratory, revealed that the water vapour absorbed continuously throughout the complete infrared spectrum, unlike the other absorbers. This special behaviour cannot be explained by line absorption based on theoretically derived line shapes like Lorentz or Voigt line shapes. For this reason it was and still is convenient to introduce an "empirical continuum" term in radiation models to account for the gap between measurements and line-by-line model results for water vapour. From a conceptual point of view the continuum is not related to a specific physical process, so that it is necessary to deal with "oversimplifications" of the water vapour line absorption. The main purpose of the continuum is to correct line-by-line models and obtain accurate results also in the window regions (Ellingson et al. 1991).

3.2.1 Dimers and clusters

The existence of this unexplained additional absorption by water vapour leads to speculations and investigations in two directions. One possible reason is absorption by dimers (Adiks et al. 1975) or even more complex clusters (Carlon 1979) of water vapour which may be generated during collisions and survive several following collisions (Suck et al. 1979). This hypothesis was supported by the negative temperature coefficient of the continuum, i.e. by the observation that the continuum effect is less for higher temperatures. This temperature behaviour is similar to the temperature dependence of making and braking of chemical bonds, like for instance bonds of dimers or clusters. Nevertheless, following the more recent studies it seems unlikely that absorption by dimers and clusters could explain the complete continuum (Clough et al. 1989). There are two main reasons against the dimer hypothesis. First, there are no spectral features in the absorption spectrum which could be attributed to dimers or clusters, and secondly the optical depth of the continuum does scale as the cube of the water vapour density while the observation shows a quadratic behaviour (Clough et al. 1992). Even though dimers or more complex clusters may exist, their concentration is too weak to explain the continuum.

3.2.2 Far wing absorption

The more favoured hypothesis assumes that the continuum is generated by the outer wings of water vapour lines. In line by line (LBL) computations, line wings are usually cut at a certain distance from the line centre, typically at $\Delta\nu \approx 10\text{cm}^{-1}$ - 20cm^{-1}. However the necessity to add an empirical continuum to any LBL model does not depend on the choice of $\Delta\nu$, as long as a Lorentz line shape is applied (Nordstrom and Thomas 1980). The assumptions behind the Lorentz line shape therefore must be reconsidered when one intends to introduce far wing effects in radiation models.

The most important assumption behind the Lorentz line shape is the impact assumption: the time τ_{free} between collisions is much longer than the time τ_{coll} spent during collisions. These approximations typically hold when the distance between the colliding molecules is much larger than their size. The interaction during such loose or streaking collisions is therefore restricted to far field effects and is generally weak (Nordstrom and Thomas 1980). Conditions during close collisions may be very different from those assumed in the derivation of the Lorentz line shape. The interaction includes near field components and the colliding molecules may build a short lived compound system. Because such collisions were neglected completely it was suspected that these close collisions which were missed in model computations could explain the empirically defined continuum. The more recent investigations aimed at the determination of the "true" line shape for water vapour absorption lines. The following four paragraphs summarize important results which were found on the way to a better understanding of the water vapour far wing absorption.

Clough et al. (1980) derived a more general line shape, following a formalism developed by Van Vleck and Huber (1977) which includes symmetrized autocorrelation functions. The molecular interaction between water vapour molecules is still restricted to the dipole-dipole interaction, but they introduced an effective finite duration of collision in the autocorrelation function and compared this against zero duration of collision as in the impact approximation. This new line shape shows Gaussian wings for non zero duration of collision instead of Lorentz wings for zero duration. The computed continuum is improved compared to the impact approximation but they still

need an empirical scaling to account for the empirical continuum. The temperature dependence was not treated.

Nordstrom and Thomas (1980) constructed a composite line shape consisting of a line shape for the near line centre region and a line shape for the far wings. The former includes the impact approximation and is essentially a Lorentz line shape scaled by frequency dependent factors which take account of the Maxwell-Boltzmann population statistics near line centres. The latter is a statistical line shape following Formin and Tvorogov (1973), which is based on the quasi static approximation, i.e. the opposite of the impact approximation. The free parameters of this far wing line shape were determined from experimental data recorded in regions where line absorption dominates. These two line shapes were superimposed by a continuous weighting function in such a way that the weight of the statistical line shape increases slowly from 0 at the line centre to 1 at a distance of 5 cm^{-1} from the line centre and vice versa for the near line centre line shape.
When they computed absorption strengths in the 10μm and 4μm window they found an excellent agreement with measurements. Furthermore a negative temperature dependence evolved from this composite line shape, although not as strong as observed. Because of this success Nordstrom and Thomas concluded that the mechanism of far wing absorption has to be considered before more exotic absorbers are introduced.

Clough et al. 1989 followed again the concept of symmetrized autocorrelation functions like they did in their 1980 study. Here they applied a frequency dependent semiempirical scaling function $\chi(\nu)$ to the Lorentz profile to account for duration of collision effects. The intention is to keep χ close to 1 in the near line centre region, where the Lorentz line shape is valid, but to vary $\chi(\nu)$ farther away from the centre in an optimal way, to reproduce the observed water vapour absorption in the atmospheric windows. The parameters of the chosen $\chi(\nu)$ function were fitted at given temperatures both for water vapour self broadening and for foreign broadening.
The semiempirical scaling function $\chi(\nu)$ at T = 296 K shows an increase from 1 at the line centre to ~10 at 25 cm^{-1} from the line centre. This super Lorentz behaviour is continued out to the far wings at ~100 cm^{-1} for foreign broadening and even to ~300 cm^{-1} for self broadening. The super Lorentz region is followed by a continued exponential decrease to very low values, with the foreign broadening $\chi(\nu)$ decaying faster than the self broadening $\chi(\nu)$. From this it is inferred that the foreign broadening contributes mainly in the spectral regions close to the strong bands, while the self broadening is the main source for absorption far away from the lines.

Ma and Tipping (1991, 1992a, 1992b) applied a comprehensive quantum mechanical formalism to describe collisions between water vapour molecules (1991 and 1992a) and collisions between a water vapour molecule and a nitrogen or carbon dioxide molecule (1992b). The main assumptions are the quasistatic approximation for the far wing limit and the binary collision approximation. The interaction consists of two parts, an isotropic interaction approximated by a simple Lennard-Jones type model and the leading anisotropic multipolar interaction. The anisotropic interaction is of the dipole-dipole and dipole-quadrupole type for collisions among water vapour molecules and for collisions between water vapour and nitrogen or carbon dioxide, respectively. An important feature of this theory is the fact that it is free of arbitrarily adjustable parameters.
The Ma and Tipping line shape contains two scaling functions $\chi_+(\nu)$ and $\chi_-(\nu)$ for the positive and negative resonance line shape functions. These scaling functions have a similar meaning as the single semi empirical $\chi(\nu)$ function of Clough et al. (1989). Although an exact comparison is not

justified it is instructive to see that Ma and Tipping's scaling functions for water vapour collisions cause an increased absorption strength in the spectral region of ~50cm^{-1} to ~300cm^{-1} from the line centre, followed by a rapid decrease in the far wings. The temperature dependence of this new line shape is clearly negative. The scaling functions for water vapour vs. nitrogen have local maxima in the same region and a steep decent towards the far wings. The temperature dependence of this latter absorption process is negative, but considerably less than in the former case. The comparison of the theoretically derived absorption in the windows is excellent in the 300cm^{-1} to 1100cm^{-1} region and at least reasonable in the following windows up to 10,000cm^{-1} where experimental data are less extensive and less accurate.

In the light of the very encouraging studies by Ma and Tipping it seems very likely that what was (and still is) designated as the water vapour continuum can be explained mostly by far wing contributions from lines in the adjacent bands of the window. So far the application of new line shapes is restricted to LBL models, but once a new line shape is established it should be a comparatively minor problem to bring its advantage into narrow band models and finally into wide band models as they are found in comprehensive climate models.

4 Water vapour absorption in ECHAM4

The ECHAM4 general circulation model contains a modified version of the Morcrette radiation scheme (Morcrette 1984). It is a nonisothermal emissivity type wide band model (=WBM) which resolves the infrared spectrum with six independent bands, three of them split in two halves, and the short wave range with only two bands. The infrared spectrum is split as follows (ordered by wave length):

- band1 : 0 - 350 cm^{-1} H_2O lines
- band 5 : 350 - 500 cm^{-1} H_2O lines + continuum
- band 2 : 500 - 800 cm^{-1} H_2O lines + continuum
- band 3a : 800 - 970 cm^{-1} H_2O lines + continuum
- band 4 : 970 - 1110 cm^{-1} H_2O lines + continuum
- band 3b : 1110 - 1250 cm^{-1} H_2O lines + continuum
- band 6a : 1250 - 1450 cm^{-1} H_2O lines
- band 1b : 1450 - 1880 cm^{-1} H_2O lines
- band 6b : 1880 - 2820 cm^{-1} H_2O lines

The line absorption is parameterized by Padé approximants for each absorber and band where the absorber is included. These parameters are found by a fit to the bandwise integrated transmissivities computed in a narrow band model (= NBM) for a range of given absorber amounts and ambient pressure values (Morcrette 1986).

The water vapour absorption is considered through all bands and consisting of a contribution by line absorption and a parameterization accounting for the empirical continuum in the window region, i.e. in the bands 5, 2, 3a, 4 and 3b (c.f. list above), reaching from 350cm^{-1} to 1250cm^{-1}. The Padé approximants parameterize the line absorption including their overlap inasmuch as it is

included in the NBM. In Morcrette's NBM the former is modelled by the Malkmus band model based on the Lorentz line shape, while the latter is achieved by a continuum like correction following Ramanathan and Downey (1986). This correction accounts for the errors occurring because of the application of the multiplication property for whole bands. The parameterization of the water vapour continuum follows Roberts et al. (1976), like it does in the NBM towards which the WBM is tuned. This continuum is described in the succeeding chapter.

4.1 Continuum parameterization by Roberts et al. 1976

This continuum absorption contains both, the e-continuum taking care of H_2O-H_2O collisions and the (p-e)-continuum accounting for H_2O-N_2 collisions. The dominating e-continuum absorption (5) is described by an absorption strength $C^o(\nu)$ for a constant temperature T=296K (4) and a temperature correction factor taking account of the strong variation of this type of continuum with temperature changes. The (p-e)-continuum is assumed to be proportional to the e-continuum at T=296K (6). This proportionality γ is supposed to be constant in the whole spectral range where the continuum is considered. Any temperature dependency of the (p-e)-continuum is neglected. The following equations are taken from the Roberts et al. paper.

$$C^\circ(\nu) = a + b \cdot exp(-\beta\nu) \tag{4}$$

$$C_e(\nu, T) = C^\circ(\nu) \cdot exp\left[T_0 \cdot \left(\frac{1}{T} - \frac{1}{296K}\right)\right] \tag{5}$$

$$C_{p-e}(\nu) = \gamma \cdot C^\circ(\nu) \tag{6}$$

Roberts et al. estimated the parameters a, b, β and T_o based on laboratory measurements for the spectral range reaching from 8µm to 30µm:

$a = 1.25 \cdot 10^{-22}\ mol^{-1}cm^2atm^{-1} = 4.18\ cm^2\ g^{-1}$ at p=1000 hPa
$b = 1.67 \cdot 10^{-22}\ mol^{-1}cm^2atm^{-1} = 5578\ cm^2g^{-1}$ at p=1000 hPa
$\beta = 7.87 \cdot 10^{-3}$ cm
$T_o = 1800$ K

It is pointed out that of the various factors affecting the continuum absorption the greatest experimental uncertainty is with N_2-H_2O absorption, i.e. in this context with γ. The LOWTRAN code which is discussed in the paper of Roberts et al. sets $\gamma = 0.005$ according to McCoy et al. (1969). Roberts et al. find that this ratio is a substantial overestimate and recommend to set γ between 0.002 and 0.

However, it is meanwhile well known from measurements that this ratio depends on the frequency (Burch and Gryvnak, 1980). The magnitude of γ changes substantially from ~ 0.01 at 400cm^{-1} to ~ 0.001 in 800cm^{-1} to 1250cm^{-1} within the atmospheric window where this parameterization is applied.

4.2 The continuum in ECHAM4

The Morcrette scheme is a wide band model and therefore computes the continuum absorption bandwise. This implies an averaging of the absorption strength $C^o(\nu)$ over each band, resulting in

coefficients C^0_b for a band b. The averaging process (7) formally includes a weighting function $w(\nu)$. Setting $w(\nu)\equiv 1$ allows a simple arithmetic averaging. In this report the weighting function is utilized to include the spectral dependence of the blackbody radiation in the computation of new continuum coefficients C^0_b (8).

$$C_b^0 = \frac{\int_{\nu_1}^{\nu_2} C^\circ(\nu)\, w(\nu)\, d\nu}{\int_{\nu_1}^{\nu_2} w(\nu)\, d\nu} \quad \text{, for band b} = [\nu_1, \nu_2] \tag{7}$$

$$w(\nu) = w(\nu, T) = \frac{2h\nu^3}{c^2} \cdot \frac{1}{\exp\left(\frac{h\nu}{kT}\right) - 1} \tag{8}$$

The temperature T should be chosen as a typical temperature of the lower troposphere where the continuum is the dominant absorption term in the atmospheric window

The ratio γ is defined once for all four bands where it is included. The original setting in the Morcrette radiation scheme is $\gamma = 0.002$, i.e. the upper limit of the value recommended in the Roberts et al. paper.

Once the parameters C^0_b and γ are specified, the radiation scheme computes the optical density over vertical paths, e.g between the elevations z_1 and z_2, as the sum of the single contributions (9) by the self (10) and the foreign continuum (11), and for all bands b where it is considered.

$$\tau_b^{cont}(z_1, z_2) = \tau_b^{e}(z_1, z_2) + \tau_b^{p-e}(z_1, z_2) \tag{9}$$

$$\tau_b^{e}(z_1, z_2) = Diff \cdot C_b^0 \cdot \int_{z_1}^{z_2} \left[\frac{p}{p_0} \cdot e^{T_0 \cdot \left(\frac{1}{T} - \frac{1}{296K}\right)} \cdot \frac{\varepsilon S}{1 + (\varepsilon - 1) S} \cdot S\rho \right] dz \tag{10}$$

$$\tau_b^{p-e}(z_1, z_2) = Diff \cdot C_b^0 \cdot \int_{z_1}^{z_2} \left[\frac{p}{p_0} \cdot \gamma \cdot \frac{1 - S}{1 + (\varepsilon - 1) S} \cdot S\rho \right] dz \tag{11}$$

S = specific humidity [g/g], ε = M(dry air)/M(H2O) = 1.608g/g
Diff = diffusivity factor = 1.66 (Elsasser, 1942)

Both integrals sum the water vapour mass $S\rho$ between the elevations z_1 and z_2, weighted by the relative pressure p/p_0, a temperature term (10) or γ (11) and a function of the specific humidity S. Because S is always a number much smaller than 1 this S term behaves primarily linear in S for the e-continuum but approximately like a constant factor of 1 for the (p-e)-continuum.

The e-continuum is stronger than the (p-e)-continuum wherever (12) holds. The T-scaling term is usually between 1 and 10, c.f. table 1, and S in the range of 1mg/kg to 10g/kg.

$$\Gamma(T, S) = e^{T_0 \cdot \left(\frac{1}{T} - \frac{1}{296K}\right)} \cdot \frac{\varepsilon S}{1 - S} > \gamma \tag{12}$$

The (p-e)-continuum term surpasses the e-continuum firstly in dry air and secondly in warm air. Therefore the former must be important in deserts, which are dry by definition, or in very cold conditions, where the specific humidity is low due to the low temperature.

TABLE 1. Some typical values taken by the T-scaling in EQ10

T [°C]	-45.0	-30.0	-15.0	0.0	15.0	30.0
T-scaling	6.10	3.75	2.44	1.66	1.18	0.87

4.2.1 Modification of the continuum band coefficients C^0_b

In a first series the original coefficients were compared with sets evolving from (7), without temperature weighting ($w(\nu)\equiv 1$), and with temperature weighting (8) for three different temperatures T = 250K, 270K, 290K. The ratio γ was set to 0.002 for all bands including the continuum. Hence both continuum terms are modified simultaneously and equally in each band, c.f. (10) and (11), with exception of band 2. The original scheme contains separate definitions of C^0_2 for the e- and the (p-e)- continuum. The effect of unequal coefficients in band 2 is a modification of the prescribed parameter γ by a factor of (112./12.)=9.3, i.e. the effective value for γ_2 is 0.019 instead of 0.002. The resulting coefficients and the JJM-coefficients are displayed in table 2. The new C^0_b parameters are considerably stronger in the water vapour window (band 5 and 2), but similar in the following bands 3 and 4.

TABLE 2. New continuum coefficients C^0_b for specified weighting (7 and 8), with the values of the original scheme (JJM) shown in addition

	b=2	b=3	b=4	b=5
w(ν,T)≡1	46.0	7.53	5.82	213.
T=250K	48.6	8.48	5.87	210.
T=270K	47.7	8.31	5.87	209.
T=290K	47.0	8.16	5.86	208.
JJM	12. / 112.	6.25	5.	80.

These sets of continuum coefficients were put into the longwave radiation model of ECHAM4-L19 to test the effect of these changes on the radiative boundary fluxes for atmospheric standard profiles given by McClatchey et al. (1971). McClatchey and colleagues defined typical profiles of temperature, ozone and humidity for different latitude belts and seasons. The mixing ratio of carbon dioxide is set to 300ppm. In this test the computations are carried out for the tropical case, the mid latitude summer case and the sub arctic winter case, which are referred to as TRO, MLS and SAW cases respectively. The SAW case has necessarily the driest humidity profile of these three cases.

The table 3 shows the resulting fluxes for the three McClatchey profiles TRO, MLS and SAW. It contains the surface downward flux, the outgoing longwave radiation at the top and the net flux at the tropopause. These fluxes are computed for the continuum coefficients as found in the original scheme (JJM) and as derived for uniformly weighted band averaging ($w(n,T)\equiv 1$) and for temperature depending band averaging. The fluxes are omitted for the combinations of TRO plus 250K temperature weighting and SAW plus 290K temperature weighting.

TABLE 3. LW fluxes for TRO, MLS and SAW profiles [W/m^2].

	JJM	$w(\nu,T)\equiv 1$	T=250K	T=270K	T=290K
TRO: F^d_{surf}	-392.4	-400.0	--	-402.4	-402.0
TRO: F^u_{top}	301.0	298.9	--	298.4	298.5
TRO: F^n_{tropop}	292.0	289.7	--	289.2	289.3
MLS: F^d_{surf}	-344.8	-352.0	-354.5	-354.0	-353.6
MLS: F^u_{top}	290.5	289.0	288.6	288.7	288.8
MLS: F^n_{tropop}	275.5	274.0	273.6	273.7	273.7
SAW: F^d_{surf}	-164.3	-166.0	-166.3	-166.2	--
SAW: F^u_{top}	203.1	203.0	203.0	203.0	--
SAW: F^n_{tropop}	183.5	183.4	183.4	183.4	--

The table shows a remarkable increase in the surface downward flux F^d_{surf} for all of the new continuum coefficients sets against the JJM-coefficients. The differences between F^d_{surf} for JJM-coefficients and F^d_{surf} for $w(\nu,T)\equiv 1$ is 7.4W/m^2, 7.2W/m^2 and 1.7W/m^2 for TRO, MLS and SAW, respectively. Taking the difference between F^d_{surf} for the temperature weighted sets with T= 290K for TRO, T=270K for MLS and T=250K for SAW, and F^d_{surf} for the JJM-set one finds even stronger increases: 9.6W/m^2, 9.2W/m^2 and 2.0W/m^2. The sensitivity of F^d_{surf} to the weighting temperature is relative small. Changing T from 250K to 290K causes an absolute difference of only 1.0W/m^2, 0.9W/m^2 and 0.2W/m^2 for TRO, MLS and SAW.

The changes in the outgoing longwave radiation F^u_{top} and in the net flux F^n_{tropop} at the tropopause are considerably smaller, because the water vapour continuum is mainly a tropospheric phenomenon with respect to the other absorbers. Both fluxes are weaker for the new coefficients. The differences between F^u_{top} for the JJM-coefficients and F^u_{top} for the temperature weighted coefficients (T=290K for TRO, T=270K for MLS and T=250K for SAW) are: 2.5W/m^2, 1.8W/m^2 and 0.1W/m^2. The corresponding differences of F^n_{tropop} are: 2.7W/m^2, 1.8W/m^2 and 0.1W/m^2. The sensitivities of these two fluxes to the weighting temperature is likewise small.

A replacement of the JJM-coefficients by any of the other coefficient sets clearly increases the counterradiation at the surface and reduces the net flux at the tropopause and the upward flux at the top. All of these effects are more pronounced in the TRO and MLS case than in the SAW case.

Whether temperature weighting is applied or not is much less important than the step away from the original coefficients. If temperature weighting is applied it is fair to use a constant temperature, e.g. T=270K, for all cases, since the sensitivity to this parameter is small.

Figure 2 shows the cooling rates for all tests. The cooling rates are generally intensified in the lower troposphere with respect to the case with original coefficients. The strongest increase is approximately 0.4K/day for TRO, 0.2K/day for MLS and 0.04 for SAW. The differences between the cases with or without temperature weighting are very small.

4.2.2 Modification of γ

In a second test the continuum coefficients C^0_b were held fixed and the parameter γ was varied, i.e. the e-continuum remained unchanged while the (p-e)-continuum changed linearly in γ. The continuum coefficients C^0_bwere chosen from table 2 for a weighting temperature of T=270K. The computations were carried out for four different settings of γ, as pictured in Figure 3.

- γ=0.002 for all bands, as recommended as an upper limit in Roberts et al. 1976.
- γ=0.005 for all bands, as applied in McCoy et al. 1969
- $\gamma = \gamma_b$=bandwise average over the theoretically derived γ-values in Ma and Tipping 1992b:

  350 - 500 cm-1 : γ_5 = 0.059
  500 - 800 cm-1 : γ_2 = 0.017
  800 - 970 cm-1 : γ_3 = 0.0025
  970 - 1110 cm-1 : γ_4 = 0.0018
  1110 - 1250 cm-1 : γ_3 = 0.0025

- $\gamma = \gamma_b$=bandwise average over γ-values derived by Burch, for the bands 5 and 2 (as listed in Ma and Tipping 1992b). The ratio for the bands 3 and 4 is set to 0.002, since there are only a few measurements:

  350 - 500 cm-1 : γ_5 = 0.031
  500 - 800 cm-1 : γ_2 = 0.012
  800 - 970 cm-1 : γ_3 = 0.002
  970 - 1110 cm-1 : γ_4 = 0.002
  1110 - 1250 cm-1 : γ_3 = 0.002

The downward flux at the surface, the upward flux at the top and the net flux at the tropopause are presented in table 4 for TRO, MLS and SAW, respectively.

TABLE 4. LW fluxes for TRO, MLS and SAW profiles [W/m^2]. The columns one and two are computed for a spectrally uniform ratio γ. The results in columns three and four are derived for bandwise defined ratios γ_b

	γ = 0.002	γ = 0.005	$\gamma = \gamma_b$(M&T)	$\gamma = \gamma_b$(B)
TRO: F^d_{surf}	-402.4	-407.0	-403.3	-402.8
TRO: F^u_{top}	298.4	296.3	292.6	294.5
TRO: F^n_{tropop}	289.2	287.1	283.5	285.3

TABLE 4. LW fluxes for TRO, MLS and SAW profiles [W/m^2]. The columns one and two are computed for a spectrally uniform ratio γ. The results in columns three and four are derived for bandwise defined ratios γ_b

	$\gamma = 0.002$	$\gamma = 0.005$	$\gamma = \gamma_b$(M&T)	$\gamma = \gamma_b$(B)
MLS: F^d_{surf}	-354.0	-358.8	-355.6	-355.0
MLS: F^u_{top}	288.7	287.0	282.2	284.7
MLS: F^n_{tropop}	273.7	271.9	267.8	269.7
SAW: F^d_{surf}	-166.2	-169.3	-176.4	-174.3
SAW: F^u_{top}	203.0	202.7	200.3	201.3
SAW: F^n_{tropop}	183.4	183.1	180.7	181.7

A spectrally uniform increase of γ from 0.002 to 0.005 intensifies F^d_{surf} by 4.6W/m^2, 4.8W/m^2 and 3.1W/m^2 in the cases TRO, MLS and SAW. F^u_{top} is diminished by 2.1W/m^2, 1.8W/m^2 and 0.3W/m^2 respectively. F^n_{tropop} changes almost equally like F^u_{top}.

The two cases with bandwise defined γ values behave remarkably different with respect to the two former cases with γ values fixed over all bands. The subsequent discussion concentrates on the case derived from Ma and Tipping's theoretical γ values and compares it to the γ=0.002 case.

The downward flux is increased for all McClatchey profiles like in the former cases. The changes for TRO (0.9W/m^2) and MLS (1.6W/m^2) are modest in contrast to the SAW case with a surprisingly high increment of 10.2W/m^2. The net flux at the tropopause and the outgoing longwave radiation get diminished even stronger than for the γ=0.005 test which caused the strongest surface counterradiation. The decrease of F^u_{top} amounts to 5.8W/m^2, 6.5W/m^2 and 2.7W/m^2 for TRO, MLS and SAW, respectively. The corresponding changes of F^n_{tropop} are: 5.7W/m^2, 5.9W/m^2 and 2.7W/m^2.

Figure 4 shows the cooling rates for the four WBM computations and additionally the cooling rates as they were computed by Schwarzkopf and Fels (19??) in the GFDL-LBL model. These LBL results like others have often been used as a reference for band models. But one has to remind that this particular LBL model applies the Roberts continuum with γ fixed to 0.002.

The former pair with a fixed γ is again significantly different from the latter pair with bandwise defined γ values. The following comparison concentrates on the two "extreme" cases γ=0.002 and γ=γ_b(M&T).

In the latter of these two cases there is an increased cooling in the middle troposphere for all McClatchey cases, and a diminished cooling in the lower troposphere. The maximum difference found in the middle troposphere is: +0.6K/day, +0.5K/day and +0.4K/day for TRO, MLS and SAW. The corresponding maximum difference in the lower troposphere is -0.5K/day, -0.4K/day

and -0.1K/day. Thus, the comparison of the cooling profiles shows that the maximum cooling in the TRO and MLS cases is shifted from the lower to the middle troposphere, leaving just a local maximum of cooling where the maximum for γ=0.002 is located. The SAW case shows mainly an increase of the cooling in the middle troposphere, but only a small change below. The changes may tend to reduce the stability of the troposphere. In the tropics this possibly implies an intensification of deep convection. In the arctic winter one expects an increased surface temperature.

Finally it is interesting to compare the new cooling profiles with the GFDL-LBL cooling profiles. The new profiles are a better approximation in the lower troposphere, especially in the tropics. The reason for this is the very different vertical resolution and representation of the vertical profiles in the GFDL scheme and the ECHAM4-T42-L19 in this part of the atmosphere. In the middle troposphere the old profiles match considerably better. However, one has to keep in mind that this LBL model includes the Roberts continuum with a spectral uniform γ. For this reason the credibility of such LBL-cooling profiles has to be reconsidered as long as the water vapour absorption, specifically the continuum absorption, is not treated in a more satisfactory way.

4.2.3 Combination of both modifications

This paragraph compiles results from three of all combinations listed in the tables above, in order to demonstrate the change of fluxes between the original continuum parameterization, an intermediate version and a new parameterization, which are named cases A, B, and C, respectively.

- A: The reference parameters equal to the original scheme, i.e.:
  C^0_b = JJM-coefficients from table 2, $\gamma = 0.002$
- B: The intermediate case, i.e.:
  C^0_b = coefficients for T=270K in table 2, $\gamma = 0.002$
- C: The new parameterization, i.e.:
  C^0_b = coefficients for T=270K in table 2, $\gamma = \gamma_b$(M&T) as defined in 4.2.2

The first step, from A to B, includes a change of the continuum parameters C^0_b, the second step from B to C a replacement of the ratio γ. The results for these three cases and the differences C-B and C-A are compiled again in tables 5 for the McClatchey profiles TRO, MLS and SAW.

TABLE 5. LW fluxes for TRO, MLS and SAW profiles [W/m^2]. The columns one to three show results derived with the original continuum parameters (A), an intermediate parameter set (B) and the ECHAM4 parameter set (C), respectively. The columns four and five contain the flux differences C-B and C-A. Upward fluxes are positive.

	Case A	Case B	Case C	C-B	C-A
TRO: F^d_{surf}	-392.4	-402.4	-403.3	-0.9	-10.9
TRO: F^u_{top}	301.0	298.4	292.6	-5.8	-8.4
TRO: F^n_{tropop}	292.0	289.2	283.5	-5.7	-8.5
MLS: F^d_{surf}	-344.8	-354.0	-355.6	-1.6	-10.8
MLS: F^u_{top}	290.5	288.7	282.2	-6.5	-8.3
MLS: F^n_{tropop}	275.5	273.7	267.8	-5.9	-7.7

TABLE 5. LW fluxes for TRO, MLS and SAW profiles [W/m^2]. The columns one to three show results derived with the original continuum parameters (A), an intermediate parameter set (B) and the ECHAM4 parameter set (C), respectively. The columns four and five contain the flux differences C-B and C-A. Upward fluxes are positive.

	Case A	Case B	Case C	C-B	C-A
SAW: F^d_{surf}	-164.3	-166.2	-176.4	-10.2	-12.1
SAW: F^u_{top}	203.1	203.0	200.3	-2.7	-2.8
SAW: F^n_{tropop}	183.5	183.4	180.7	-2.7	-2.8

The comparison shows a distinct qualitative difference between the warm cases TRO and MLS, and the cold case SAW, especially in the behaviour of F^d_{surf}. For the warm cases one finds that the modification of the C^0_b -coefficients causes most of the change in F^d_{surf} (TRO: (C-B)/(C-A)=8.3%, MLS: (C-B)/(C-A)=15%), while the modification of γ is equally important for F^u_{top} (TRO: (C-B)/(C-A)=69%, MLS: (C-B)/(C-A)=78%) and F^n_{tropop} (TRO: (C-B)/(C-A)=67%, MLS: (C-B)/(C-A)=77%). In the cold case all flux changes are almost entirely due to the modification of γ: (F^d_{surf}: (C-B)/(C-A)=84%, F^u_{top}: (C-B)/(C-A)=96%, F^n_{tropop}: (C-B)/(C-A)=96%).

These tests indicate that the revised C^0_b -coefficients have a major effect on the LW downward flux at the surface and a moderate effect on the LW net tropopause flux and the OLR when applied to a warm atmosphere. The γ modification has a strong effect on all of the listed fluxes in a cold and therefore dry climate and further it accounts for the major part of the flux changes at the top and the tropopause in warm conditions.

5 Validation of model results

All computations presented so far were carried out for the idealized McClatchey profiles. This chapter compares model results for the continuum versions A, B and C, as defined above, with observations.

The comparison is made for the LW downward surface flux. The computations are carried out for observed profiles of temperature and humidity and compared against the fluxes observed at the same date and place. The observed profiles of temperature and humidity are interpolated to the 19 standard levels of ECHAM4. The ozone profile and the aerosol load are taken from the ECHAM4 climatologies for the actual geographical location of the station. The CO_2 volume mixing ratio is set to 353ppm and the trace gases CH_4, N_2O, CO and CFCs are set to climatological values as specified in ECHAM4.

The observation data are taken from the Baseline Surface Radiation Network (BSRN) data base which is coordinated in the World Radiation Monitoring Network (WRMC) run by the Division of Climate Sciences, Department of Geography, ETH Zürich (Gilgen et al., 1993). Observations were available from three stations: Greenland, Payerne (Switzerland) and Von Neumayer (Antarctica).

The Greenland data were obtained in a summer field campaign in 1991. Payerne and Von Neumayer station are regular BSRN stations. The comparison was restricted to clear sky cases, i.e. to cases with 0/8 overcast.

The accuracy of the data is rather difficult to estimate, since it depends not only on the apparatus but also on the weather conditions. The main problems are firstly the SW radiation which has to be shielded off during day, and secondly the determination of clear sky conditions during night. Typical instrument errors thus may occur in the range of ± 10 W/m^2 (Wild et al., 1995). Following the same paper LW fluxes are often underestimated at daytime.

5.1 Greenland station at 69.6°N, 49.3°W

The dataset contains 16 measurements taken in spring and summer 1991. Figure 5a shows the model results on the ordinate against the observed fluxes on the abscissa. The frame has a main diagonal, where computation=observation, and dashed side diagonals with an offset of 10W/m^2 and 20W/m^2 to both sides. Points below the diagonal indicate that the model fluxes are smaller than the observed fluxes. Circles are used for model fluxes computed with the original parameterization A and crosses are used for the parameterization C (both as defined above).

It is obvious that the case A fluxes are too low. All circles but one lie below the -10 W/m^2 diagonal. Further this sample seems to be split in two subsamples, the first one containing all points below observed 240W/m^2 and slightly below the -10 W/m^2 diagonal, the second one containing points above observed 220W/m^2 and well below the -20 W/m^2 diagonal. The two subsets, both with 8 points, have a common subdomain of observed fluxes between 220W/m^2 and 240W/m^2. A simple statistics of the differences A-obs., C-obs. and C-A is compiled in table 6. It presents means and variances for the total sample and for the subsamples 1 and 2.

TABLE 6. Greenland statistics, means in W/m^2, variances in W^2/m^4.

	A-obs.	C-obs.	C-A
mean(all)	-20.5	-7.11	13.4
var(all)	53.4	54.8	0.28
mean(1)	-13.9	-0.29	13.6
var(1)	8.5	7.4	0.43
mean(2)	-27.1	-13.9	13.2
var(2)	4.1	3.7	0.08

The C-A differences have very similar means for the complete sample and both subsamples. These means are comparable to the C-A difference computed for the SAW case. The variances are very small. It follows that the effect of the new continuum parameterization is almost uniform within the given domain of temperature and humidity profiles. However, the comparison of the A-obs. and C-obs. variances shows that the variances within the single subsets are considerably less than the pooled variance. The means as well support the impression that there is a bias of appr. 13W/m^2

between the observations in subsample 1 and subsample 2. This splitting is very clear in the histogram in the figures 6a and 6d showing the differences A-observation and C-observation. Speculations about the reason for this splitting are postponed to the discussion of the Von Neumayer data. However, the case C computations are in excellent agreement with the observations in subsample 1 and the differences C-obs. are only about half as big as the differences A-obs.

5.2 Payerne 46.8°N, 7.0°E

The dataset contains 25 observations taken in 1988 and 1989. The model computations and observations are represented in figure 5b and simple statistics for the complete sample are listed in table 7. Figures 6b and 6e show the A-observation and C-observation histograms. Both histogram have a sharp dominant peak centred at 2.1W/m^2 (C-obs.) and -9.4W/m^2 (A-obs.). The largest positive case C differences occur for computations, where the observations are higher than 300W/m^2. The largest negative differences are found for case A computations between 280W/m^2 and 300W/m^2.The differences C-A are again very uniform.

TABLE 7. Payerne statistics, means in W/m^2, variances in W^2/m^4.

	A-obs.	C-obs.	C-A
mean(all)	-9.4	2.12	11.5
var(all)	47.3	42.7	0.67

The domain of the Greenland subsample 2, i.e. the range from 220W/m^2 to 270W/m^2, shows a favourable agreement between Payerne case C computations and observations. This is another hint that the subsample 2 of the Greenland data is probably confound by some process not included in the radiation scheme.

5.3 Von Neumayer station at 70.65°S, 8.25°W

The dataset has 35 measurements taken in 1992 and 1993. Figure 5c, 6c and 6d, and table 8 show the data, the histograms and the statistics. Generally all computations underestimate the observations, especially in the upper half ranging from observed 180W/m^2 to 230W/m^2, where the agreement in the Greenland and Payerne data was very good. This offset seems to be present throughout the complete sample and is strongest above 200W/m^2. The histograms have two peaks, but they are not separated as clearly as in the Greenland histograms. Nevertheless, it is remarkable that the separation between the peaks is 13W/m^2 in both stations. A subjective division of the full sample in two subsamples gives a first subsample of 25 events, where C-obs.$\leq$-12W/m^2, and a second subsample of 10 events above this level. The subsample 1 has C-obs. centred at appr. -21W/m^2,

the subsample 2 at -7W/m^2. The variance of both subsamples is necessarily strongly reduced compared to the variance of the full sample.

TABLE 8. Von Neumayer statistics, means in W/m^2, variances in W^2/m^4.

	A-obs.	C-obs.	C-A
mean(all)	-29.0	-15.6	13.4
var(all)	43.7	43.2	0.65
mean(1)	-32.3	-19.0	13.2
var(1)	17.9	14.4	0.69
mean(2)	-20.7	-7.0	13.7
var(2)	10.9	10.0	0.45

Once more, the difference C-A is almost constant, like in the two former datasets, and the amplitude of 13.4W/m^2 is very similar to the corresponding value for Greenland data.

As mentioned above, there is a surprising parallel between the two arctic stations, inasmuch as the errors of the computations have a bimodal histogram instead of a distribution with a single dominating peak like in the Payerne data. In both stations the peaks are separated by appr. 13W/m^2. Therefore it is tempting to assume that a process which occurs only in polar regions under some meteorological conditions is missed by the model.

Such an effect could be caused by the presence of small ice crystals in otherwise clear air as it is reported in Curry et al. (1990). This paper contains radiative transfer computations for two cases where the actual ice-crystal size spectra were measured from aeroplanes. The first case was chosen as a typical winter case with an ice crystal extinction coefficient of τ_{ext}=5.3, the second case a typical spring case with an ice crystal extinction coefficient of τ_{ext}=0.36. Thus the ice-crystals build an opaque layer in the former, but only a weakly absorbing layer in the latter case. Therefore, it may be assumed that the second case would get a 'clear sky' classification, and hence this spring case could be similar to some of the 'clear sky' observations used in the Greenland and Von Neumayer sections.

The computations were carried out with and without consideration of the ice-crystal load. In the winter case the LW net surface flux drops dramatically from 83.8W/m^2 (clear air) to 5.1W/m^2 (with ice). The effect is very similar to the presence of fog or a low level cloud. In the spring case the LW net surface flux drops from 76.7W/m^2 (clear air) to 61.1W/m^2 (with ice), i.e. the ice-crystal forcing is -15.6W/m^2. This value is very similar to the difference between the two peaks in the Greenland and Von Neumayer histograms. After all, this gives some evidence to the hypothesis that the ice-crystals are the main cause for the differences between observed and computed fluxes in the Greenland subsample 2 and Von Neumayer subsample 1. Ice-crystals in otherwise clear air are completely neglected in the radiation code as used in this study.

6 Implications for ECHAM4 winter climate

The preceding chapter describes tests of modified continuum parameterizations in a stand alone radiation model. The following discussion presents possible effects on the atmosphere in a January integration of the complete ECHAM4-T42-L19 general circulation model. From what has been found above it is expected that the largest impact occurs firstly in areas which are usually cloud free, and secondly in areas with a low absolute humidity. Therefore, one expects significant changes of the LW downward surface flux in deserts and in high latitudes where the humidity is low due to the low temperatures.

The following comparison comprises the continuum parameterizations A and C as they have been described above. The experiments consisted in perpetual January integrations over seven months. The months two to seven served to estimate January averages of the fields of interest. The subsequent discussion covers mainly the differences in the LW downward flux at the surface and the surface temperature on land or ice. The main purpose is to find whether the expectations which are based on single column computations are valid in a full GCM integration. In a first step the difference fields are presented and simple statistics of large scale area means are discussed. In the second step it tried to discriminate regions where the altered parameterization may play an important role from other areas where the internal variability is strong.

6.1 Longwave downward flux at the surface

The fields given by the experiments A and C and the difference field of this variable are shown in figure 7. The difference field has large amplitudes exceeding 20 W/m^2 in Africa north of the equator, in Saudi Arabia, in Pakistan, across large parts of Asia and in Antarctica. The flux over the oceans increases in most region by 0 to 10 W/m^2. Flux increases by 10 to 20 W/m^2 occur in the central Pacific south of the equator (and south of the ITCZ), across the equatorial Atlantic and in the southern Indian Ocean. Negative flux differences have amplitudes between 0 and -10 W/m^2, with exception of a few grid points, and have a much lesser extent.

Area means of the flux differences are listed in table 9 for the entire globe (*global*), the northern extratropics (*N-30*), the tropics (*30-30*) and the southern extratropics (*30-S*). *L&S* indicates averaging over land and sea, *L* stands for averaging over land only and *S* for averaging over sea only. The columns contain the corresponding values for the continuum parameterizations denoted A and C, respectively, the difference C-A between these cases and their average (A+C)/2.

TABLE 9. $-F^d_{surf}$, [W./m^2] averaged over all latitudes, the northern extratropics 90°N-30°N, the tropics 30°N-30°S and the southern extratropics 30°S-90°S, and averaged over land and sea, over land and over sea grid points.

	A	C	C-A	(A+C) / 2
global(L&S)	326.1	334.5	8.4	330.3
N-30(L&S)	233.6	244.1	10.5	238.9
30-30(L&S)	382.7	391.4	8.7	387.1
30-S(L&S)	305.3	310.9	5.6	308.1
global(L)	264.3	279.0	14.7	272.0

TABLE 9. $-F^d_{surf}$, [W./m^2] averaged over all latitudes, the northern extratropics 90°N-30°N, the tropics 30°N-30°S and the southern extratropics 30°S-90°S, and averaged over land and sea, over land and over sea grid points.

	A	C	C-A	(A+C) / 2
N-30(L)	196.8	212.4	15.6	204.6
30-30(L	345.9	360.4	14.5	353.2
30-S(L)	211.3	223.6	12.3	217.5
global(S)	350.3	356.2	5.9	353.3
N-30(S)	268.8	274.5	5.7	271.6
30-30(S	394.8	401.6	6.8	398.2
30-S(S)	320.9	325.4	4.5	323.1

The fluxes in experiment C are systematically higher than in experiment A, as it is expected. The global average is raised by 8.4 W/m^2, similar to the increase in the tropics (8.7 W/m^2). The increase in the northern extratropics (10.5 W/m^2)is almost double of that in the southern extratropics(5.6 W/m^2). Further it is obvious that the flux intensification is much stronger over land surfaces, where the means are between 12.3 and 15.6 W/m^2, than over sea surfaces where the differences reach only 4.5 to 6.8 W/m^2.

The monthly mean time series of the experiments A and C are generally well separated. Both time series are (1,1)-recurrent at the average (A+C)/2 (as listed in table 9) for all area means but N-30(S). This area mean is only (5/6,5/6) recurrent. From this simple statistics it may be tempting to conclude that the differences over land are significant at least at the 90% level. However one has to remind the extremely small size of the samples and should not draw final conclusions from this recurrence analysis.

In order to get a better insight in the role of the altered continuum parameterization it is useful to discriminate areas where this modification has to be regarded to explain flux differences from other regions where other mechanisms could contribute a considerable part too. Two such reasons are:

- Cloud effects.
- Differences in the airmasses as for instance in temperature or humidity. Such differences could occur when the difference in the circulation changes the advection to a specific region.

Therefore the following analysis tries to isolate regions where the cloudiness is small, humidity is low, temperature is high and the differences in the circulation are minor. These conditions favour a strong direct effect by the modified continuum (see chapter 4.2), and it is reasonable to assume that this mechanism is responsible for flux changes in such regions.

Figure 8 presents the total cloud cover and the LW downward flux at the surface. Panel a) shows the flux in isolines and areas where the total cloud cover is above 60% are shaded. Panel b) shows total cloud cover in isolines and areas are shaded where the flux difference is stronger than 20 W/m^2. The first panel demonstrates that only the areas between the equator and 40°N from Africa to India have high flux differences and are outside of the shaded areas, while for instance the large flux anomaly in northern Russia, where the flux difference is in excess of 30 W/m^2, are coincident with a total cloud cover higher than 90% (c.f. panel b). In Antarctica the cloud cover is below 60% in most places and the flux differences are generally between 10 and 20 W/m^2 with exception of a few grid points near 60°W. Similarly the flux differences are near 10 W/m^2 in the US where the total cloud cover is below 60% in the south and along the Rocky Mountains.

The vertically integrated specific humidity is depicted in figure 9 with the same shading as in the top panel of figure 8. This field has low values of 10g/m2 or less over all land surfaces north of 40°N and south of 60°S, and in the tropics from northern Africa to north west India. From these areas most of those north of 40°N are cloud covered by at least 60%.

The 850 hPa temperature average (A+C)/2 is shown in figure 10. Temperatures are shown in isoline and areas are shaded where the total cloud cover is higher than 60% or the vertically integrated specific humidity is higher than 20g/m^2. From those areas where the vertically integrated specific humidity and total cloud cover are low it is again the band from northern Africa to north west India where the temperatures are highest. The temperatures in the unshaded areas in the US are less favourable and Antarctica is coldest having temperatures in the range of -10 to -20°C.

Following these three criteria, i.e. total cloud cover, vertically integrated specific humidity and temperature, one may conclude that the atmospheric conditions for a comparatively large direct impact of the modified parameterization are most favourable in northern Africa, the Arabian peninsula and from Iran to north west India. That's indeed where the flux differences are largest within the tropics (c.f. figure 8a). In the US and in Antarctica only two of the conditions are favourable which is in accordance with a lower flux increase compared to the former tropical areas. In all other regions it is unclear up to which extent the continuum modifications is responsible for the flux difference

The strong flux difference in northern Russia, where the total cloud cover is near 90%, is probably due to the different strength of the zonal advection of warmer and moister air. Zonal advection of warmer air is important where the temperature isolines cross the shaded areas in an approximate north south direction. This is indeed the case in the area from Scandinavia to Siberia near 120°E, as it is shown in figure 11. The panel presents the averaged 850 hPa temperature field in isolines and areas are shaded where the zonal wind difference is stronger than 1.5 m/s. Most shaded areas are on sea. The only large shaded area on land is stretched from northern Russia to Alaska. Hence it seems like the stronger zonal advection of warm air from Europe is at least partly responsible for the increased LW downward flux in the high latitudes of Russia and Siberia.

6.2 Surface temperature on land and ice

The surface temperature fields are presented in figure 12a-c. The difference field is shown over land and ice. The surface temperature over open sea equals the prescribed SST and hence cannot change. The shading indicates relative warmings or coolings stronger than 2K.

The main feature of the difference map is certainly the temperature increase across the whole of Siberia with a maximum of 10K near (60°E,65°N). Northern Africa is 2 to 4K warmer, Saudi Arabia up to 6K, and North America about 2 to 6K warmer. Coolings occur in the Himalayas with a maximum cooling of -6K, in equatorial Africa and equatorial South America.

The amplitudes on the southern hemisphere are comparatively modest. Warmings above 3K are found in eastern Brazil, in the Namib desert and on Antarctica where the maximum of 7K is at the same place as the maximum increase of the surface flux. Antarctica is 2 to 3K warmer in most areas. Coolings take place in Argentina, east of the Andes, and in southern Africa at 20°S. The amplitude of the cooling in the former region is 2 to 3K, in the latter region 3 to 4K.

The surface temperature is subject to the same processes as the LW downward flux. Thus the same arguments as used in the preceding chapter 6.1 can help to interpret the surface temperature difference field. Thus the impressive temperature rise in Siberia is probably caused just by the stronger advection of warmer air, while the increase in the areas reaching from northern Africa to north west India seems to be a direct cause of the stronger continuum absorption. The same may hold for North America and Antarctica where the flux differences are smaller but the occuring temperature increase is in the same range as for instance in the Sahara.

7 Conclusions

The understanding of the water vapour absorption seems to be significantly better nowadays than a few years ago. The studies by Ma and Tipping may be regarded as very promising, although it has still to be shown that their line profiles can be successfully transferred to wide band models as they are required in climate research.

The tests performed in this study are basically trying to improve the continuum parameterization developed by Roberts et al. (1976). This scheme is applied in the Morcrette radiation scheme, like in many others. The computations of fluxes at the surface, tropopause and top of the atmosphere, and of cooling rates were carried out for standard profiles of temperature, humidity and ozone, as defined by McClatchey et al. (1971) for clear sky conditions.

The first series occupies itself with the derivation of band parameters for the absorption strength of the water vapour continuum. This first modification does not deal with the definition of the continuum following Roberts et al. (1976), but with the definition of band averages for this specific radiation scheme. It has been shown that when using new band parameters the surface flux gets intensified up to $10W/m^2$ for tropical conditions and mid latitude summer conditions. The increase for sub arctic winter conditions is still in the range of $2W/m^2$. The outgoing longwave radiation and the net flux at the tropopause are weakened almost equally, but much less than the downward

surface flux. The cooling rates are strengthened through the whole troposphere, but the changes are smaller than 0.4K/day for tropical conditions and smaller than 0.05K/day in sub arctic winter conditions. Thus the changes in the band parameters of the continuum leads primarily to a stronger counterradiation in warm regions, but it is unlikely that the stability of the troposphere will be affected substantially.

The second series served to investigate the sensitivity of the fluxes and the cooling rates to the ratio of the foreign continuum to the self continuum. This ratio is defined uniformly throughout the spectrum in the original continuum parameterization of Roberts et al. In a first step this ratio was raised to a higher value but still kept constant for all bands. In a second and third test the ratio was defined bandwise, in the former case based on theoretical ratios computed by Ma and Tipping, in the latter case based on ratios derived from laboratory measurements by Burch. Both of these settings involve a much higher ratio towards the low frequency end of the spectrum where the continuum is included in the radiation model. Thus the modification of γ is not just a numerical subject, but an introduction of a spectral dependency to a crucial parameter of the e-p continuum in the otherwise unchanged continuum scheme.

The effect of the first test with a ratio of 0.005 instead of 0.002 causes an increased downward flux at the surface, a diminished net flux at the tropopause and upward flux at the top, and the cooling rates are slightly increased in the troposphere. The effect of this case therefore is qualitatively very similar to the tests of the first series.

The test with bandwise defined ratios cause surprisingly different changes. The major change occurs in the sub arctic winter case, for which the surface downward flux is increased by $10W/m^2$ while the changes for tropical and for midlatitude summer conditions are considerably smaller: $0.9W/m^2$ and $1.6W/m^2$ respectively. The fluxes at the tropopause and at the top of the atmosphere are reduced strongest in the tropics and least in the sub arctic winter. The effect in the cooling rates is basically an increase in the middle troposphere and a decrease in the lower troposphere. Increase and decrease are about equal in magnitude in the tropics and in the middle troposphere, while the decrease is relatively small in the sub arctic winter case.

Observed fluxes at stations in Greenland, Payerne and Antarctica were compared with fluxes computed for observed temperature and humidity profiles. It turned out that the new scheme is in very good agreement with observations in Payerne and significantly better than the original scheme in the polar stations. The disagreement between computations and polar fluxes are presumably caused by ice crystal forcing which is not included in the radiation scheme.

Tests of the modified parameterizations in the full GCM were carried out for perpetual January conditions. The statistics of area means of the downward flux shows that the differences over land (approximately +15 W/m^2) are considerably higher then over sea (approximately +6 W/m^2). The monthly mean time series of the experiments with the old and new continuum parameterization are completely separated except over sea north of 30°N.

A more detailed analysis indicates that the increase of the LW downward flux and of the surface temperature is probably a direct cause of the stronger continuum absorption in the following areas: Africa north of the equator, the Arabian peninsula and the band from Iran to north west India, fur-

ther the US in the south and in the Rocky Mountains, and Antarctica. The large increases of flux and temperature in Russia and Siberia are at least to a substantial part caused by an intensified zonal advection of warmer and moister air from Europe, i.e. by internal variability. In other areas it is not possible to isolate single dominating processes and the changes of fluxes and surface temperature are due to internal variability, e.g. of cloud cover and advection, and to the different parameterization of the continuum.

From a numerical point of view it is important to note that the modifications do not change the cost of the integration.

Acknowledgements

The authors are indebted to the colleagues at Max-Planck-Institut für Meteorologie in Hamburg, especially to L.Bengtsson and E.Roeckner for critical discussions and careful reading of the manuscript.

Literature

Adiks, T.G., V.N. Arefev, and V.I. Dianov-Klokov, 1975, *Sov. J. Quantum Electron* **5**, 481

Burch, D.E., and D.A. Gryvnak, 1980: Continuum Absorption by H_2O vapor in the infrared and millimeter regions. In: A. Deepak, T.D. Wilkerson and L.H. Ruhnke (Editors), Atmospheric Water Vapor, Academic Press, London, 47-76

Burch, D.E., 1981: Continuum Absorption by H_2O. *Rep. AFGL-TR-81-0300*, 32 pp.

Burch, D.E., 1985: Absorption by H2O in Narrow Windows between 3000-4200cm^{-1}. *Rep. AFGL-TR-85-0036*, ? pp.

Burch, D.E., and R.L. Alt, 1984: Continuum Absorption in the 700-1200cm^{-1} and 2400-2800cm^{-1} Windows. *Rep. AFGL-TR-84-0128*, 46 pp.

Carlon, H.R., 1979, U. S. Army Armament Research and Development Command, AFCRL-TR-79013

Clough, S.A., F.X. Kneizys, R.W.Davies, R. Gamache, and R. Tipping, 1980: Theoretical Line Shape for H_2O Vapor; Application to the Continuum. In: A. Deepak, T.D. Wilkerson and L.H. Ruhnke (Editors), Atmospheric Water Vapor, Academic Press, London, 25-46

Clough, S.A., F.X. Kneizys, and R.W.Davies, 1989: Line Shape and the Water Vapor Continuum. *Atmos. Res.* **23**, 229-241

Clough, S.A., J.I. Iacondo, and J.L. Moncet, 1992: Line-by-Line Calculations of Atmospheric Fluxes and Cooling Rates: Application to Water Vapor. *J. Geophys. Res.* **97**, 15761-15785

Curry, J.A., F.G. Meyer, L.F. Radke, C.A. Brock, and E.E. Ebert, 1990: Occurence and Characteristics of Lower Troposphere Ice Crystals in the Arctic. *International Journal of Climatology* **10**, 749-764

Dicke, R.H., 1953, *Phys. Rev.* **89**, 472

Ellingson, R.G., J. Ellis, and S. Fels, 1991: The Intercomparison of Radiation Codes Used in Climate Models: Long Wave Results. *J. Geophys. Res.* **96**, 8929-8953

Elsasser, W.M., 1942: Heat Transfer by Infrared Radiation in the Atmosphere. Harvard Meteorol. Stud. 6, Harvard University Press, Cambridge, Mass.

Formin, V.V., and S.D. Tvorogov, 1973, *Appl. Opt.* **12**, 584

Gilgen, H., C.H. Whitlock, F. Koch, G. Müller, A. Ohmura, D. Steiger, and R.Wheeler, 1993: Baseline Surface Radiation Network (BSRN), Technical Plan for BSRN Data Management (Version 1.1). World Radiation Monitoring Centre Technical Report 1, WMO/TD-No. 443, 49pp.

Goody, R.M., and Y.L. Yung, 1989: *Atmospheric Radiation.* Oxford University Press, New York, 519 pp.

Kiehl, J.T., and V. Ramanathan, 1983: CO2 radiative parameterization used in climate models: Comparison with narrow band models and with laboratory data. *J. Geophys. Res.* **88**, 5191-5202

Lorentz, H.A., 1906, *Proc. R. Acad. Sci. (Amsterdam)* **8**, 591

Ma, Q., and R.H. Tipping, 1991: A Far Wing Line Shape Theory and its Application to the Water Continuum Absorption in the Infrared Region (I). *J. Chem. Phys.* **95**, 6290-6301

Ma, Q., and R.H. Tipping, 1992a: A Far Wing Line Shape Theory and its Application to the Water Vibrational Bands (II). *J. Chem. Phys.* **96**, 8655-8663

Ma, Q., and R.H. Tipping, 1992b: A Far Wing Line Shape Theory and its Application to the Foreign-Broadened Water Continuum Absorption (III). *J. Chem. Phys.* **97**, 818-828

McClatchey, R.A., R.W. Fenn, J.E.A. Selby, F.E. Volz, and J.S. Garing, 1971: Optical Properties of the Atmosphere. AFCRL-71-0279, *Environment Research Paper No. 354*, Bedford, Mass., 91pp.

McCoy, J.H., D.B. Rensch, and R.K. Long, 1969: Water Vapor Continuum Absorption of Carbon Dioxide Laser Radiation near 10μ. *Appl. Opt.* **8**, 1471-1478

Morcrette, J.-J., 1984: Sur la Paramétrisation du Rayonnement dans les Modèles de la Circulation Générale Atmosphérique. Ph.D. dissertation 630, Univ. of Lille, France

Morcrette , J.-J., 1986: Pressure and Temperature Dependence of the Absorption in Longwave Radiation Parameterizations. *Beitr. Phys. Atmosph.* **59**, 455-469

Nordstrom, R.J., and M.E. Thomas, 1980: The Water Vapor Continuum as Wings of Strong Absorption Lines . In: A. Deepak, T.D. Wilkerson and L.H. Ruhnke (Editors), Atmospheric Water Vapor, Academic Press, London, 77-100

Ramanthan V., and P.Downey, 1986: A non-isothermal emissivity and absorptivity formulation. *J. Geophys. Res.* **91**, 8649-8666

Roberts, R.E., J.E.A. Selby, and L.M. Biberman, 1976: Infrared Continuum Absorption by Atmospheric Water Vapor in the 8-12μm Window. *Appl. Opt.* **15**, 2085-2090

Rodgers, C.D., and D.C. Walshaw, 1966: The Computation of Infra-red Cooling Rate in Planetary Atmospheres. *Q. J. R. Meteorol. Soc.* **92**, 67-92

Suck, S.H., J.L. Kassner, Jr., and Yamagushi, Y., 1979: Water cluster interpretation of IR absorption spectra in the 8-14μm wavelength region. *Appl. Opt.* **18**, 2609

Van Vleck, J.H., and D.L. Huber, 1977: Absorption, emission and linebreadths: a semihistorical perspective. *Rev. Mod. Phys.* **49**, 939

Wild M., A. Ohmura, H. Gilgen, and E. Roeckner: Validation of GCM-simulated radiative fluxes using surface observations. *J. Climate* **8**, 1309-1324

Yates, H.W., and J.H. Taylor, 1960: Infrared Transmission of the Atmosphere. *NRL Report 5453 (AD 240-88)*

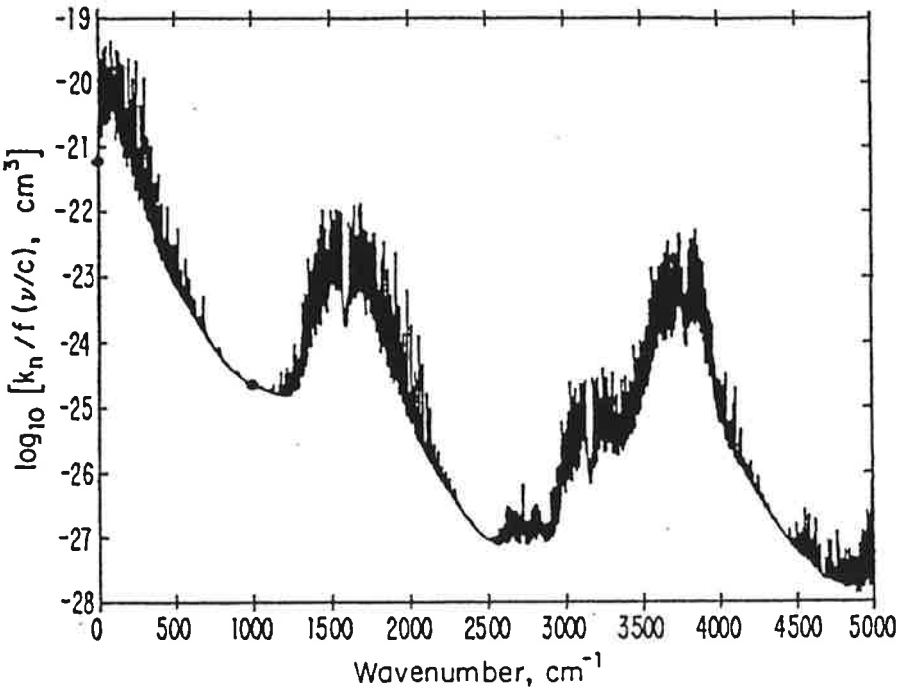

Fig. 1 Theoretical absorption coefficients for pure water vapor at 1 bar and 296 K. The vertical axis is the molecular absorption coefficient divided by a "radiation term,"

$$f(\nu/\mathbf{c}) = (\nu/\mathbf{c})\tanh(\mathbf{h}\nu/2\mathbf{k}\theta),$$

which is approximately equal to $\nu/\mathbf{c}$ (the frequency in wave numbers) for $\nu/\mathbf{c} > 500\,\mathrm{cm}^{-1}$. After Clough et al. (1980).

Fig.2: LW-cooling rates for modified continuum band parameters

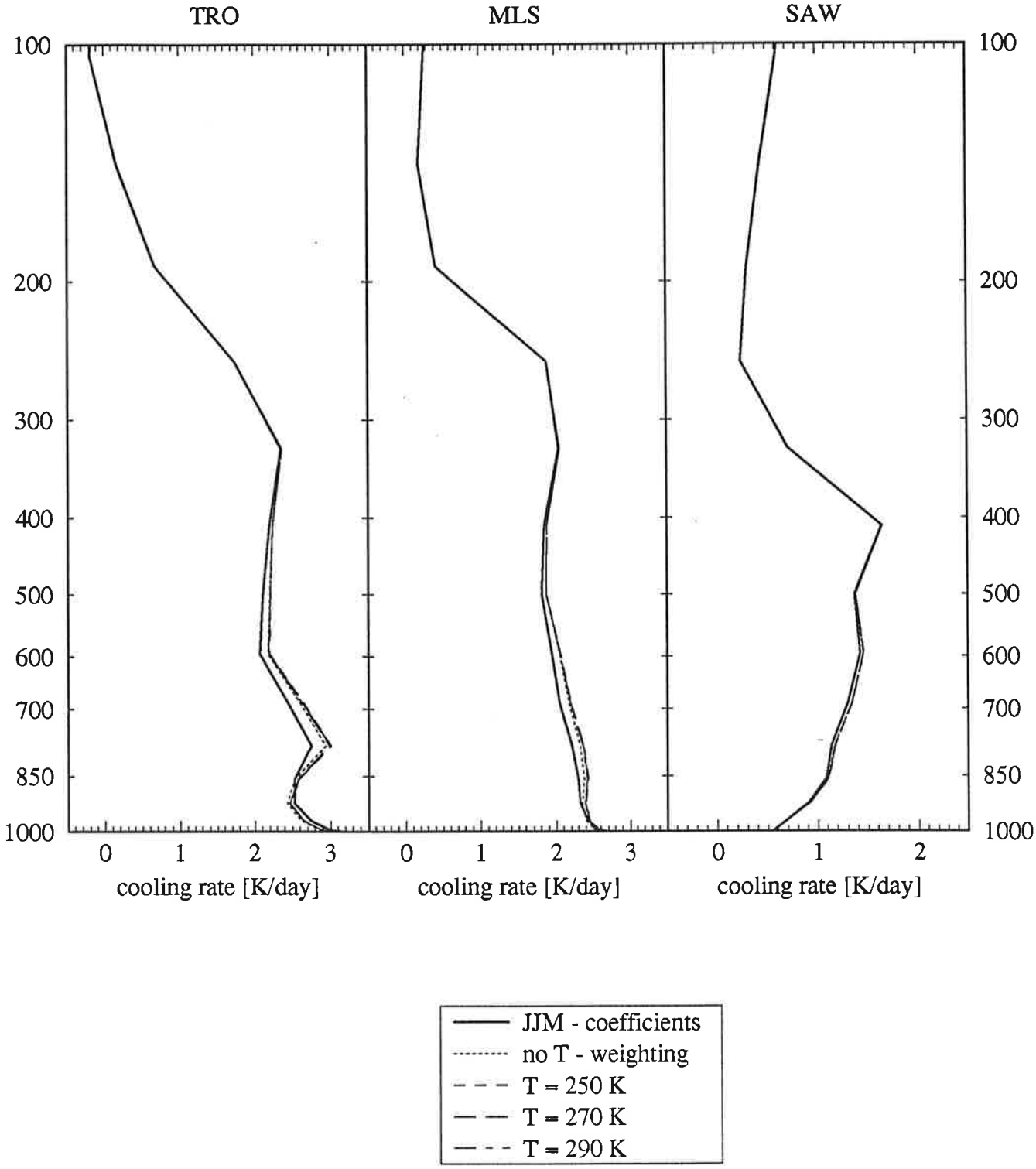

Fig.3: Cn / Cs for T=296K

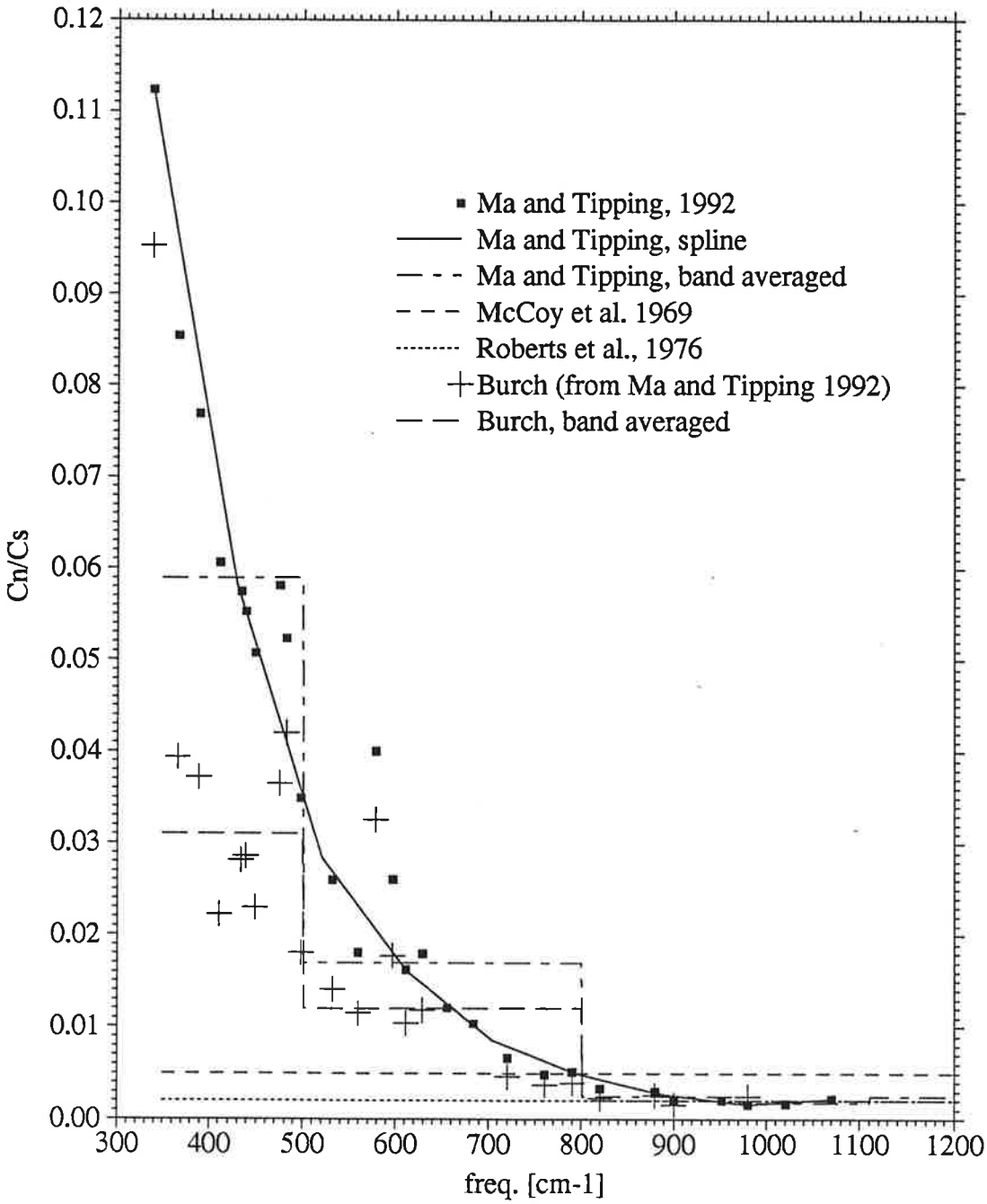

Fig.4: LW cooling rates for a modified gamma

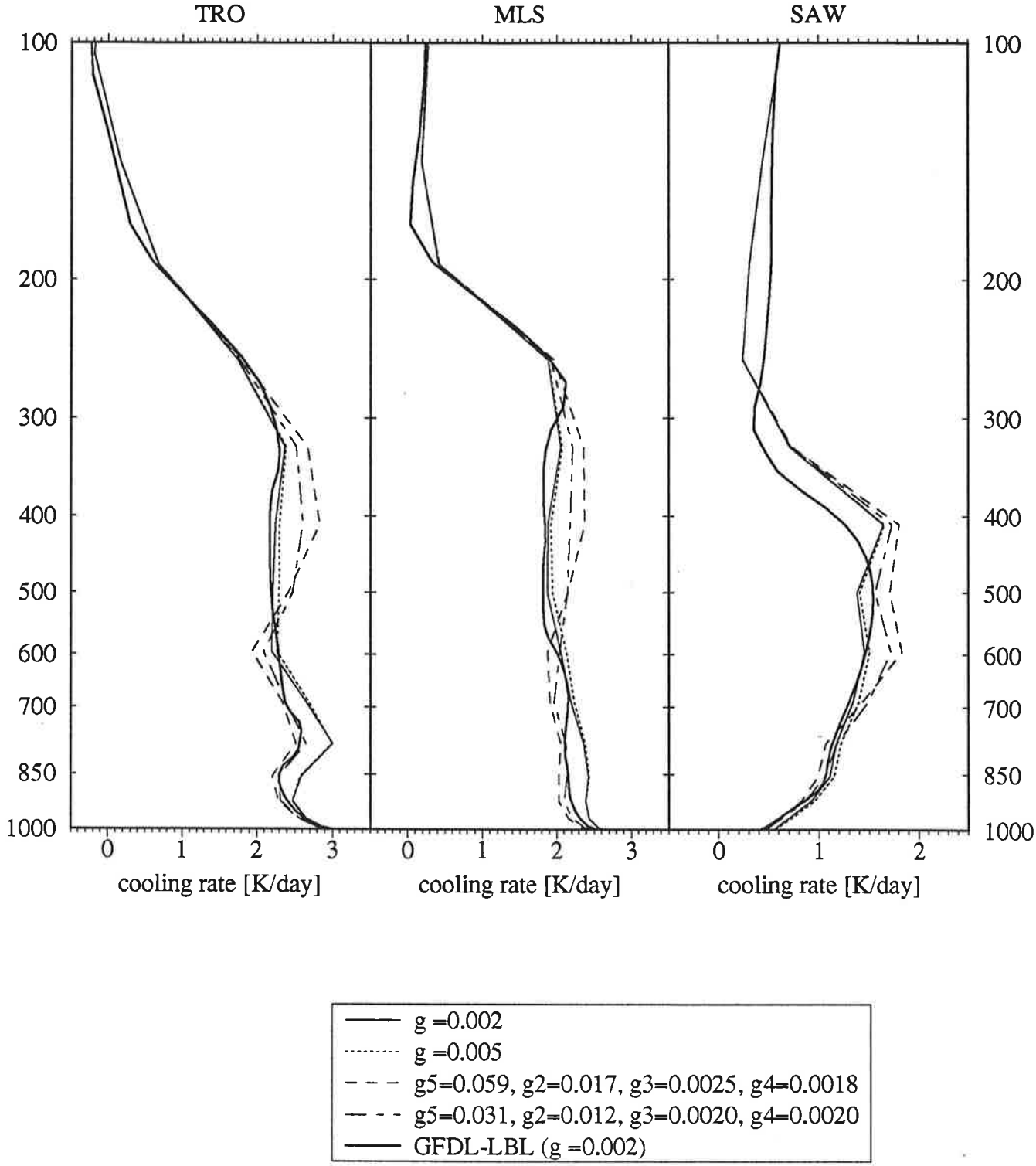

Fig.5: LW downward surface fluxes [W/m2]

a : Greenland station, x=obs., y=model

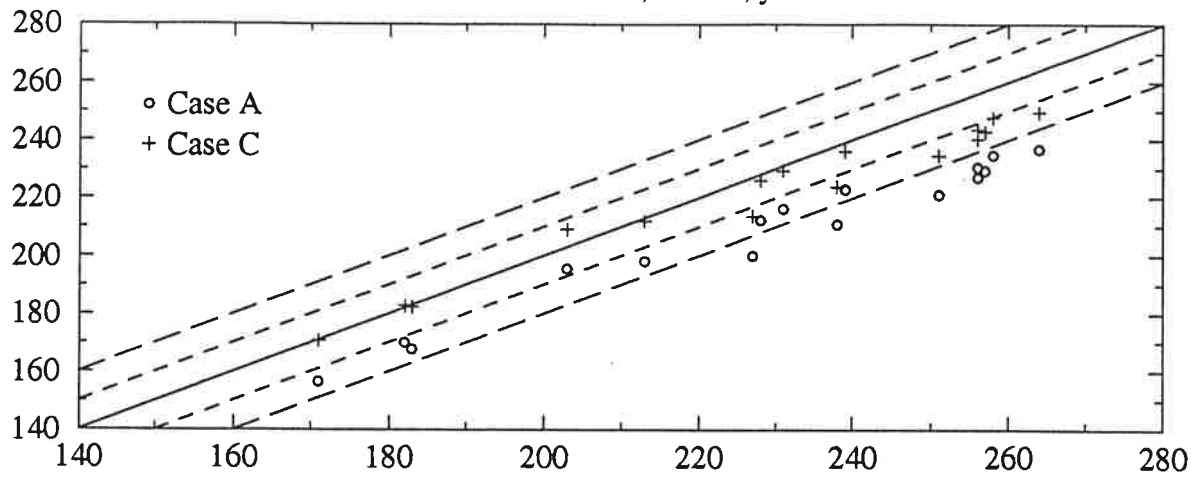

b : Payerne station, x=obs., y=model

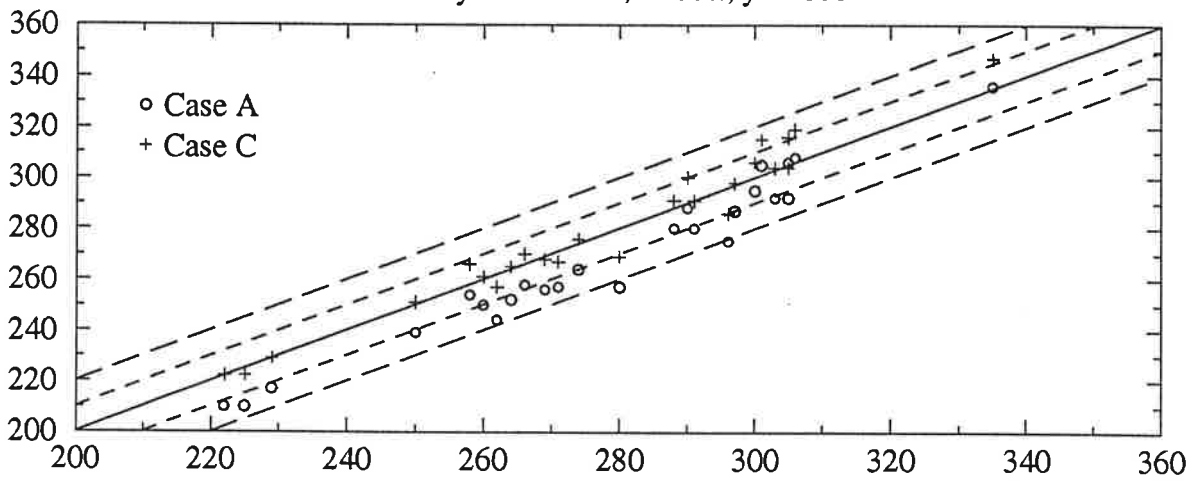

c : Von Neumayer station, x=obs., y=model

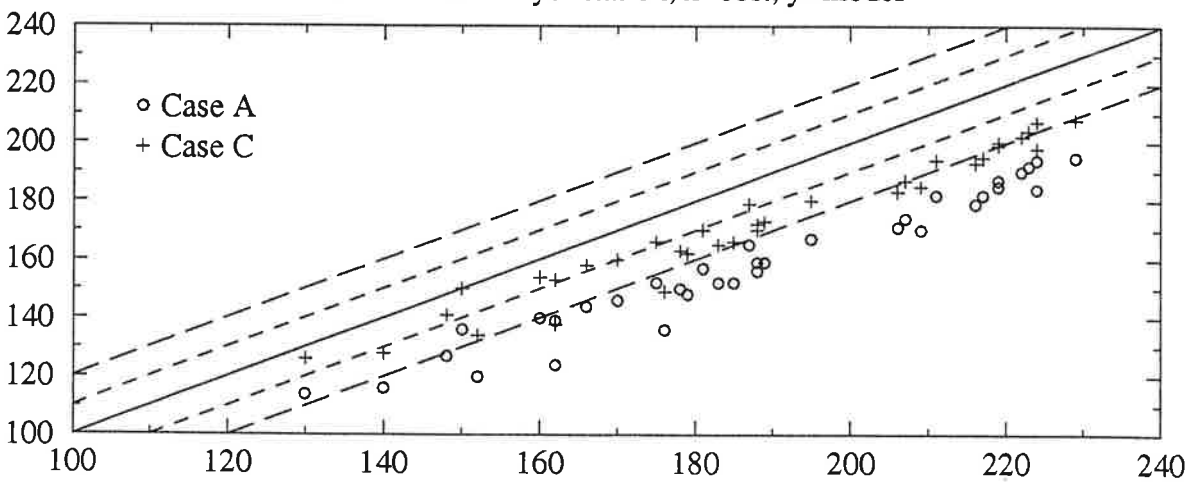

Fig.6: computation-observation histograms, bin width=3W/m2

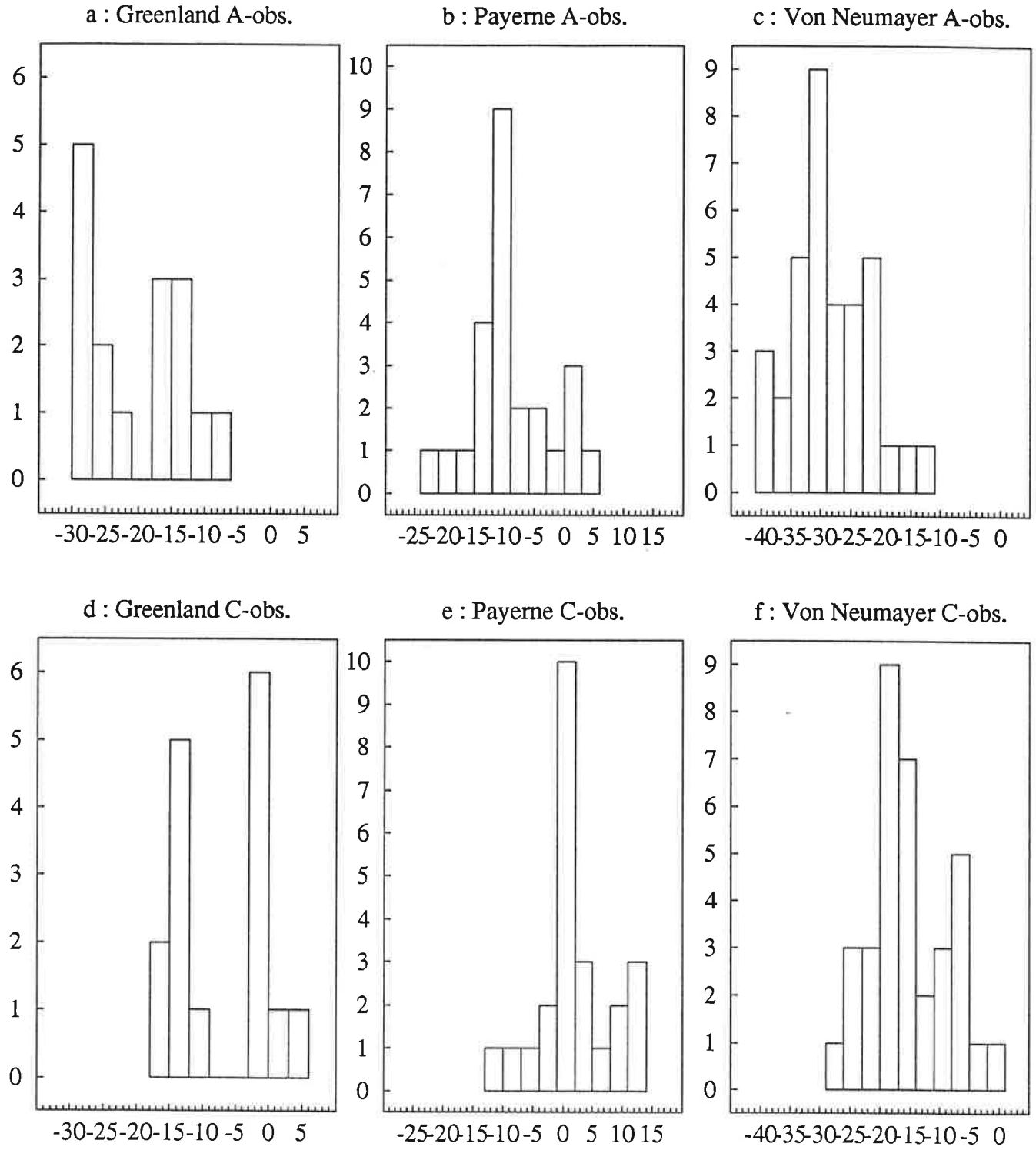

Fig.7: LW downward flux [W/m2]

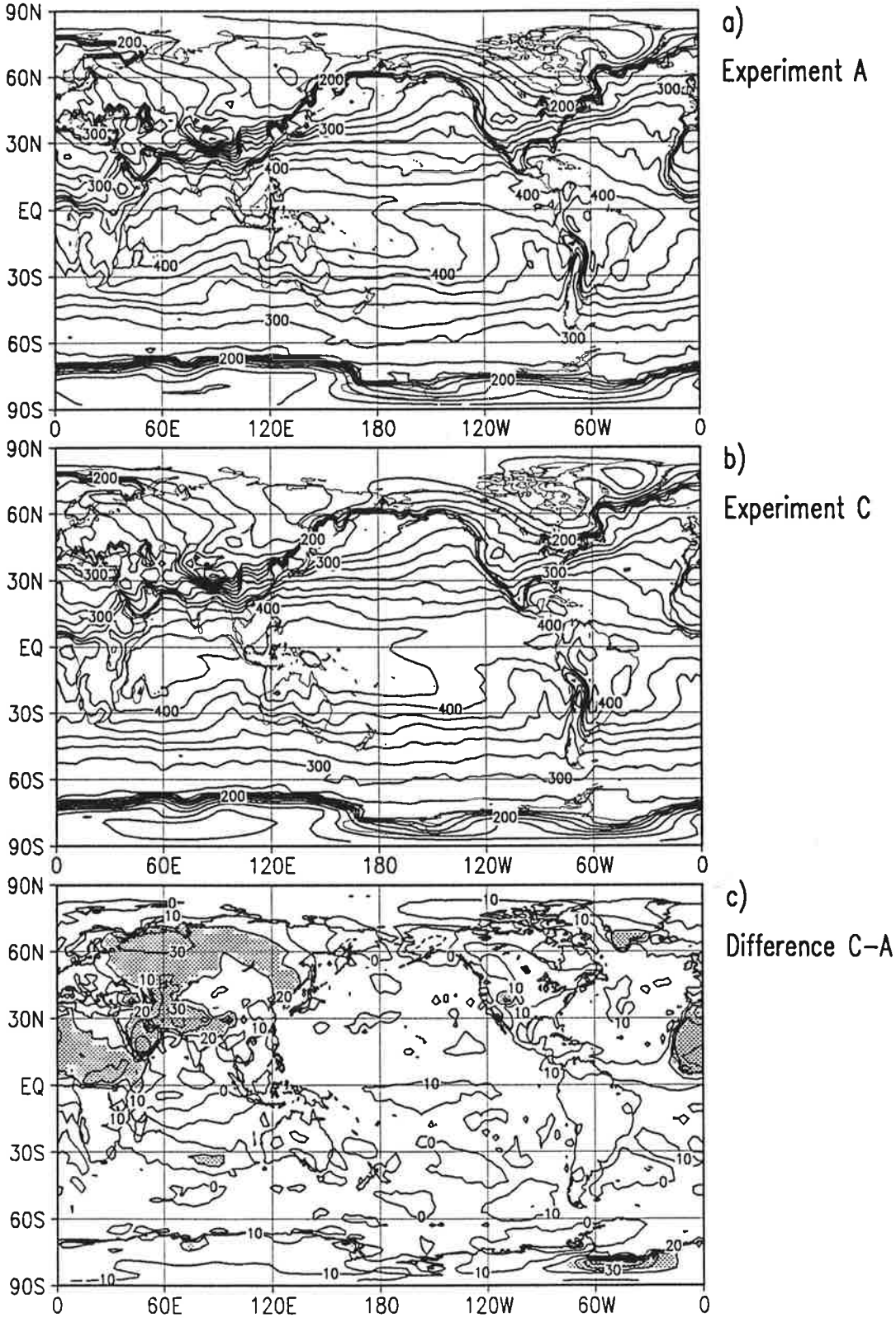

Fig.8: LW downward flux and total cloud cover

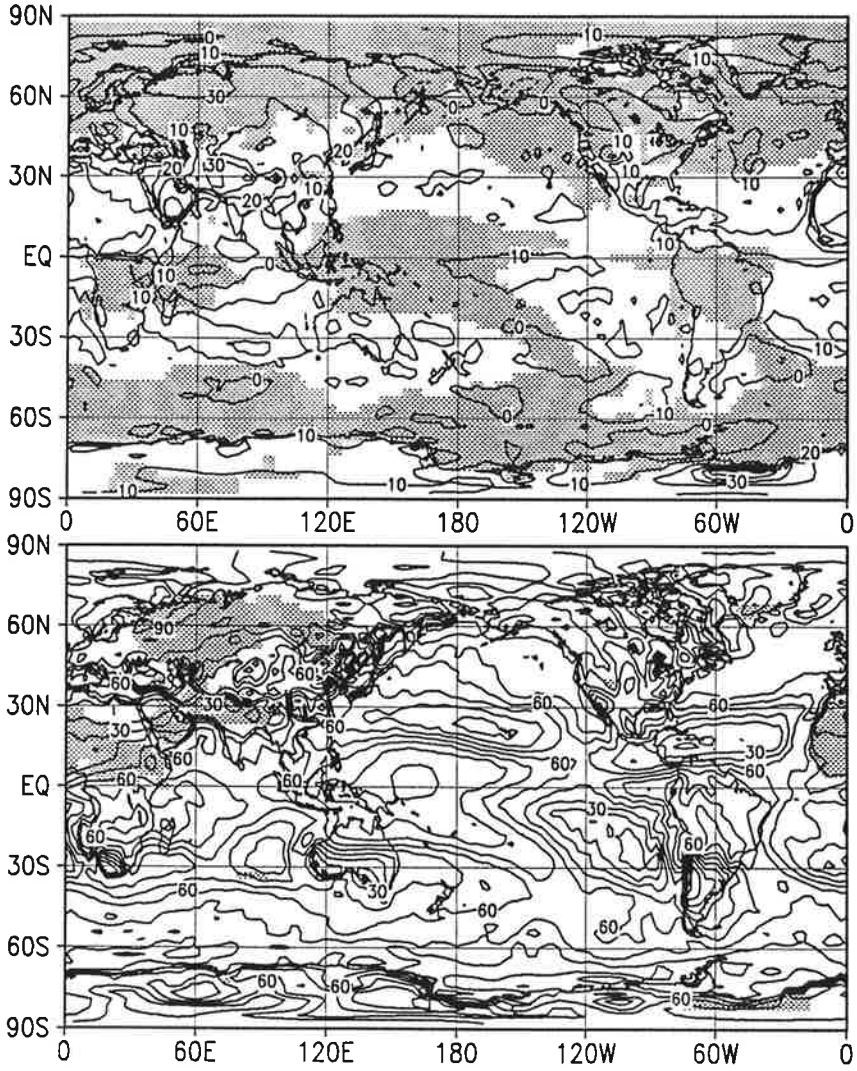

a)
Fds(C−A) [W/m2]
and total cloud cover
of (A+C)/2 where
above 60%

b)
total cloud cover [%]
and Fds(C−A) where
stronger than 20W/m2

Fig.9: vertically integrated specific humidity and total cloud cover

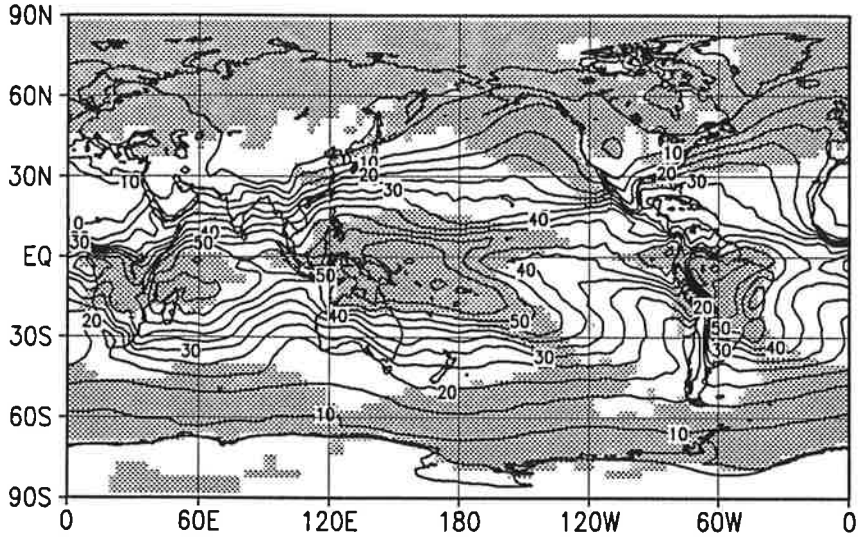

vert.integr.specific humidity [g/m2] and total cloud cover where above 60%

Fig.10: 850hPa temperature, total cloud cover and vert. integr. spec. humidity

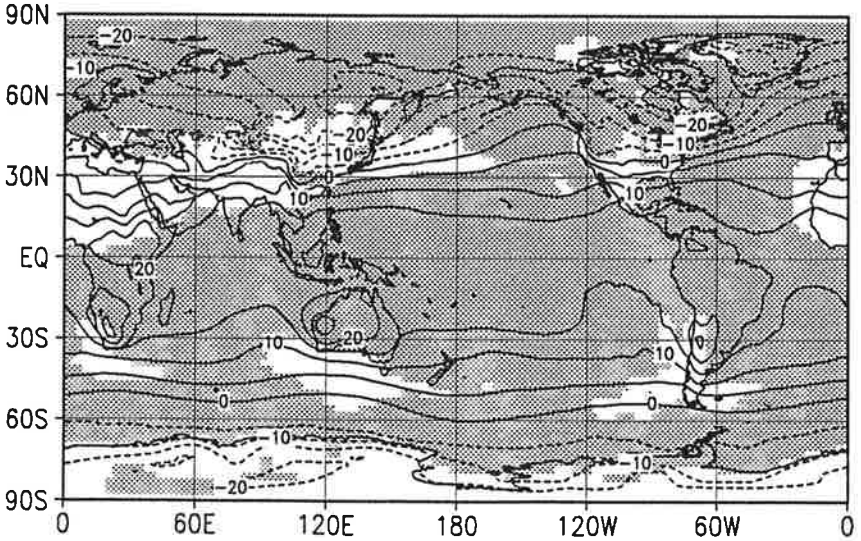

850hPa temperature [C] total cloud cover where above 60% and vert.integr.spec.hum. where above 20g/m2

Fig.11: 850hPa temperature and zonal wind difference

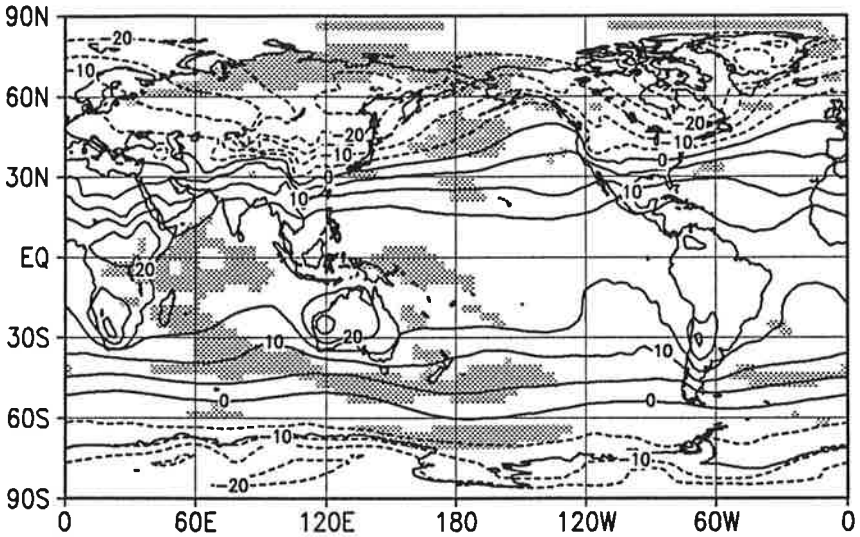

850hPa temperature [C] and 850hPa u(C−A) where stronger than 1.5m/s

Fig.12: surface temperature [C]

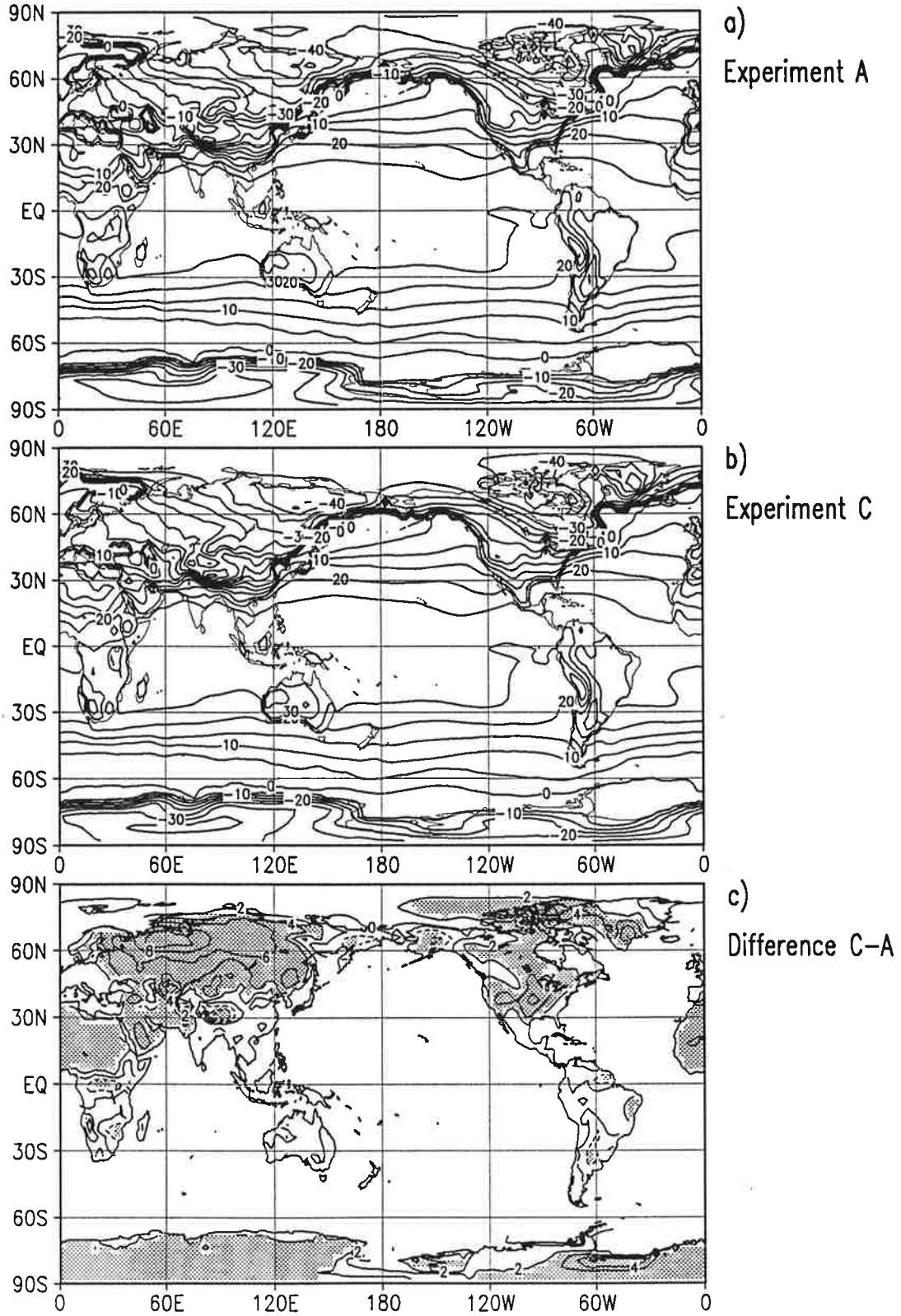

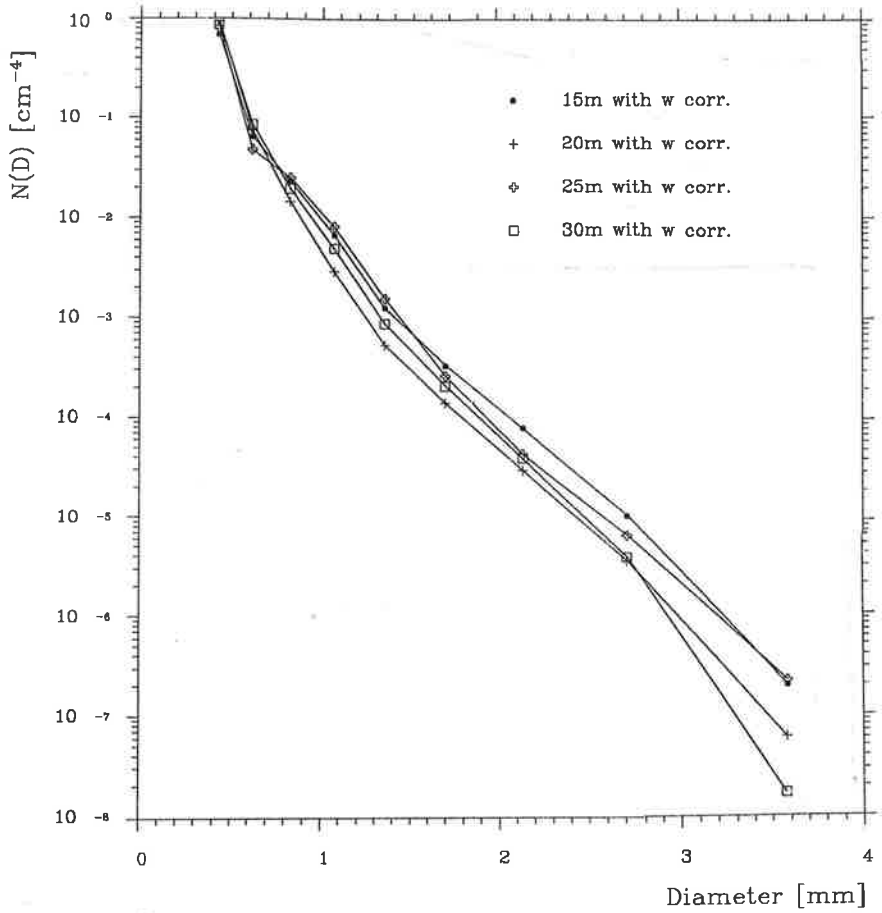

Fig.13 b: Retrieved raindrop size distribution $N(D)$ as Fig.13 a but with $\bar{w}$ correction.

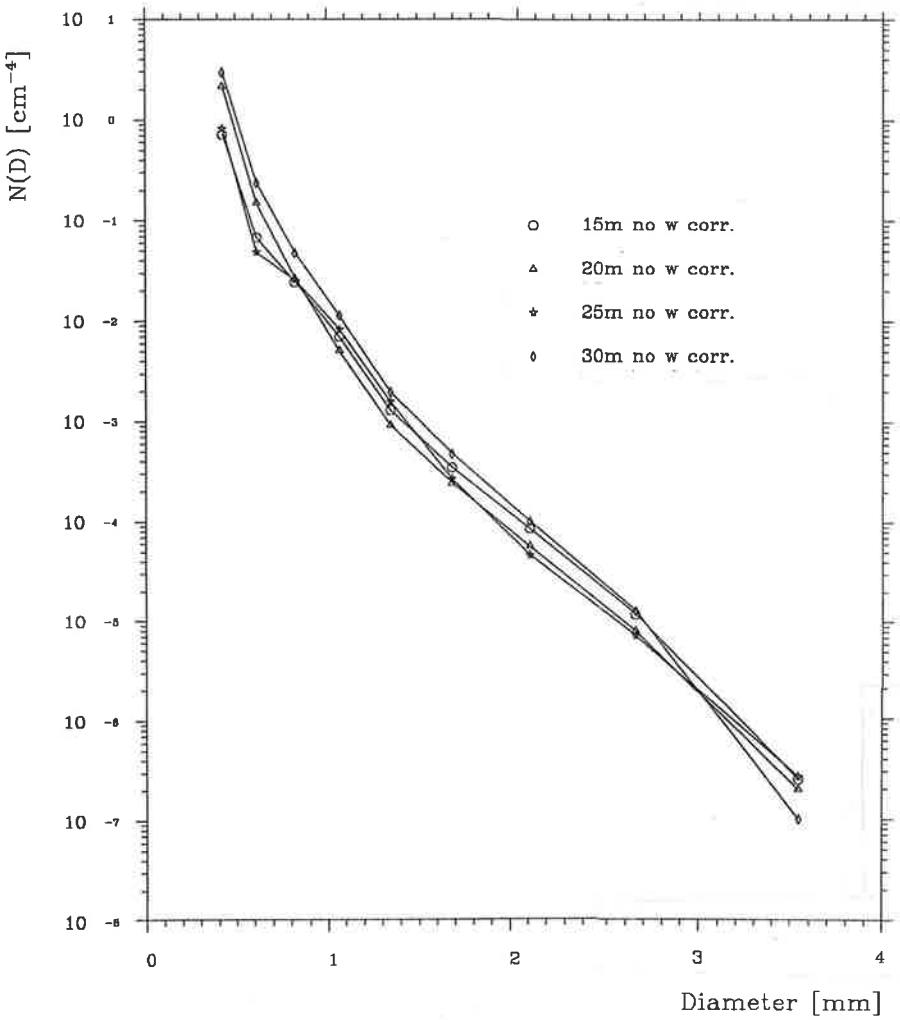

Fig.13 a: Retrieved raindrop size distribution $N(D)$ in various heights without $\bar{w}$ correction. N(D) is derived from rainfall Doppler spectra averaged over only 1 min, starting time is 012602 UTC, 6 Jan 1993.

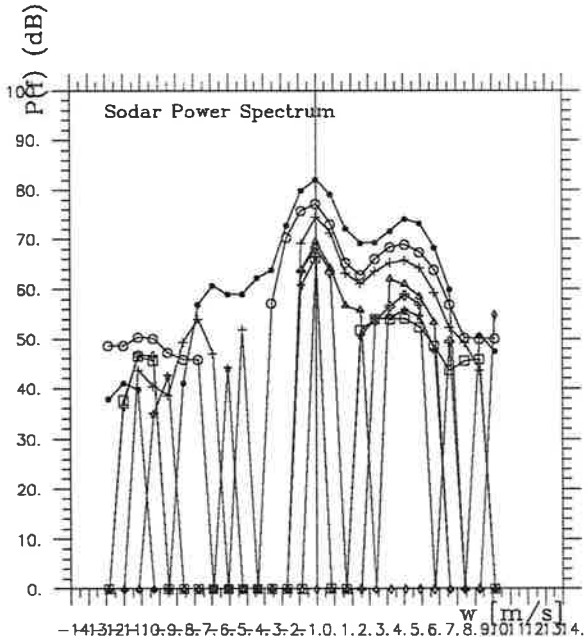
Sodar Power Spectrum
P(f) (dB)
100.
90.
80.
70.
60.
50.
40.
30.
20.
10.
0.
w [m/s]
-14 -13 -12 -11 0. -9. -8. -7. -6. -5. -4. -3. -2. -1 0. 1. 2. 3. 4. 5. 6. 7. 8. 9 10 11 12 13 14.

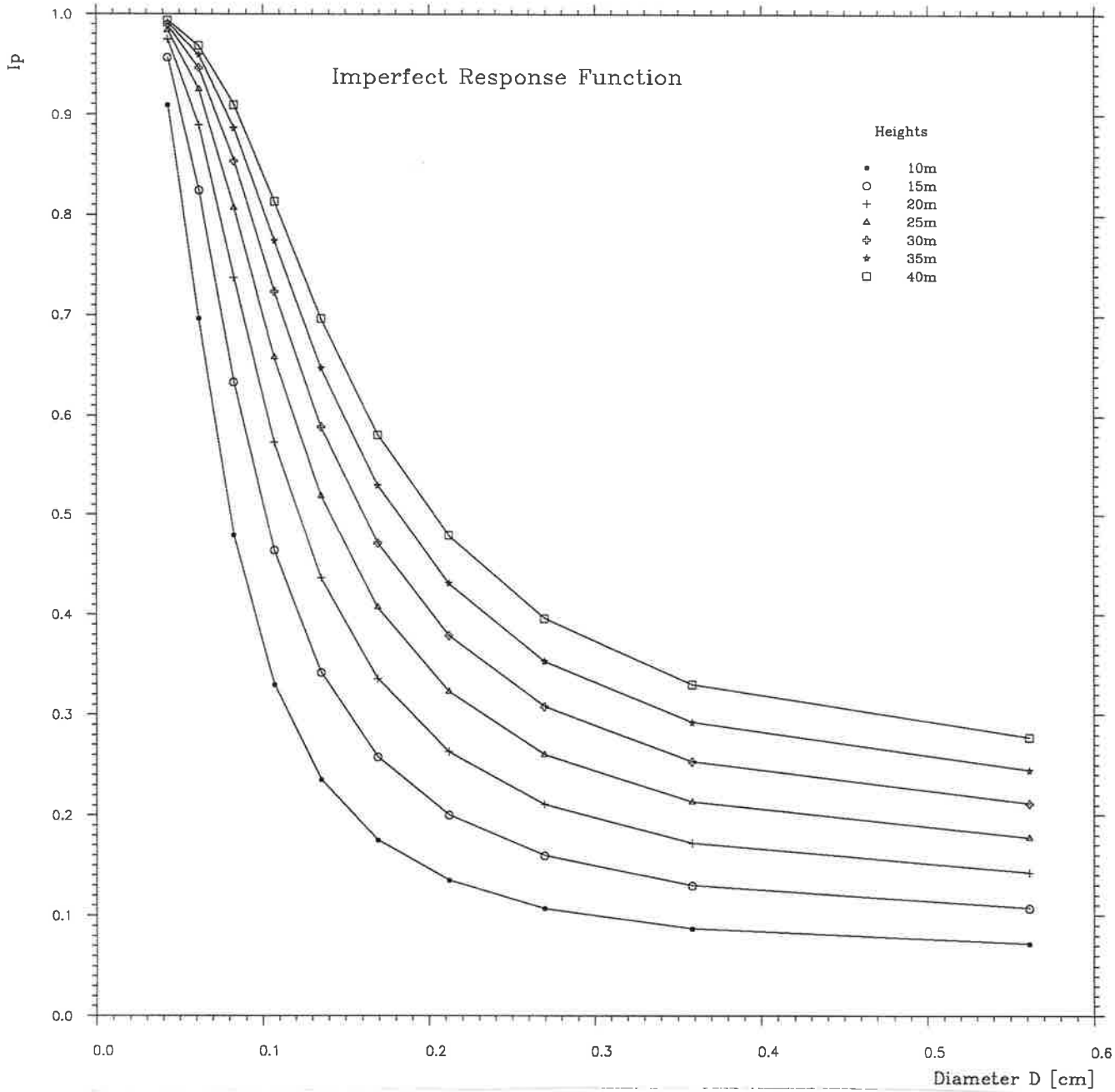

Figure 14: Imperfect precipitation response function $I_p(D, r_i)$ versus D for different turbulence intensities. Using the empirical relationship, $\lambda_a \approx 0.35 r_i$, the 7 curves correspond to different heights from 10m to 40m.

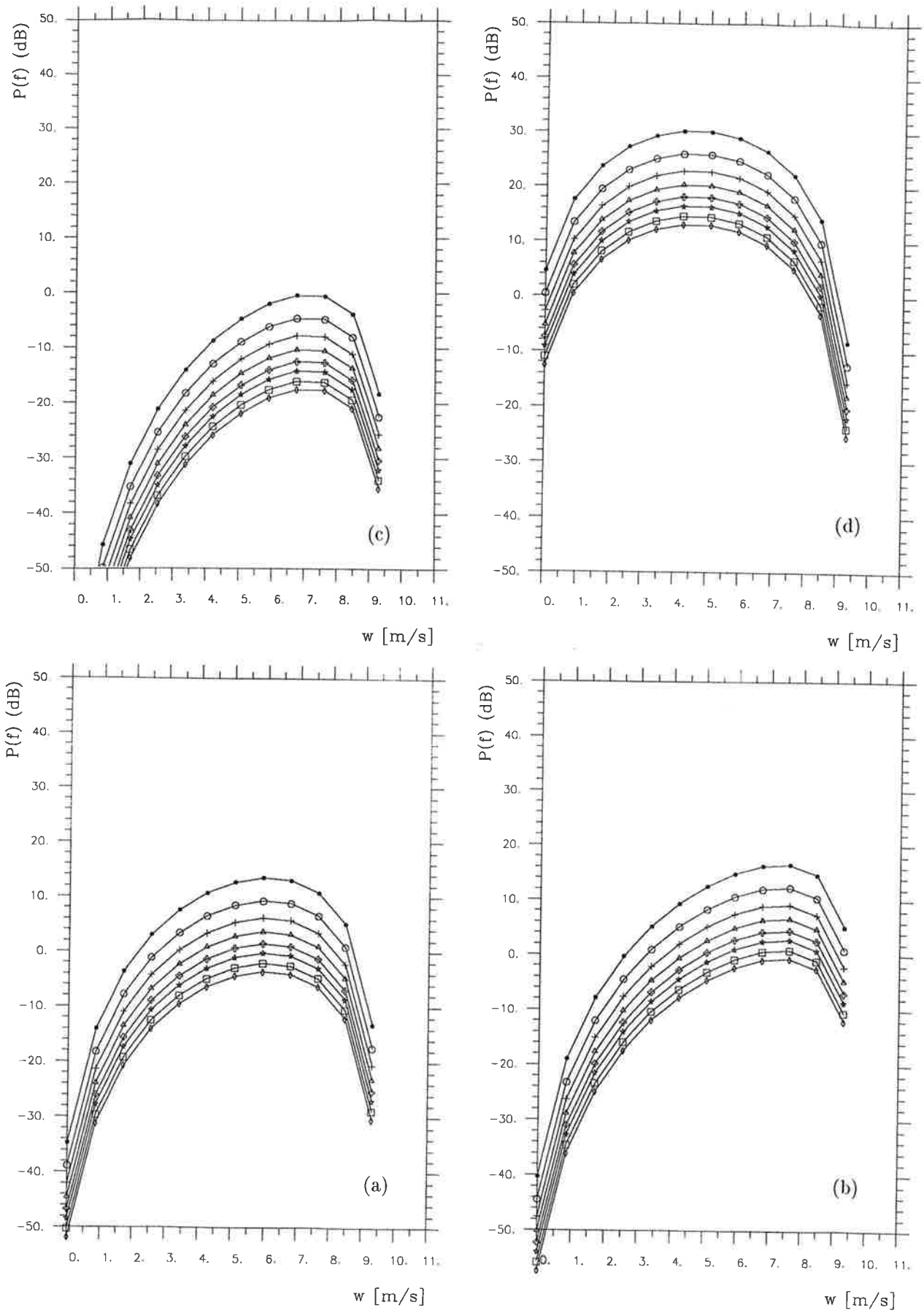

Fig.15 a-d: Simulated relative Doppler power spectra for a 6.4kHz sodar and for M-P drop size distributions with (a) $N_0 = 0.08cm^{-4}$ and $\Lambda = 40cm^{-1}$, (b) $N_0 = 0.02cm^{-4}$ and $\Lambda = 30cm^{-1}$, and Gamma distributions (c) with $N_0 = 0.08cm^{-4}$, $\Lambda = 40cm^{-1}$ and $\mu = +2$, (d) with $N_0 = 0.08cm^{-4}$, $\Lambda = 40cm^{-1}$ and $\mu = -2$.
The temperature profile assumed is linear with 0^oC in 10m to $+3.5^oC$ in 45m.

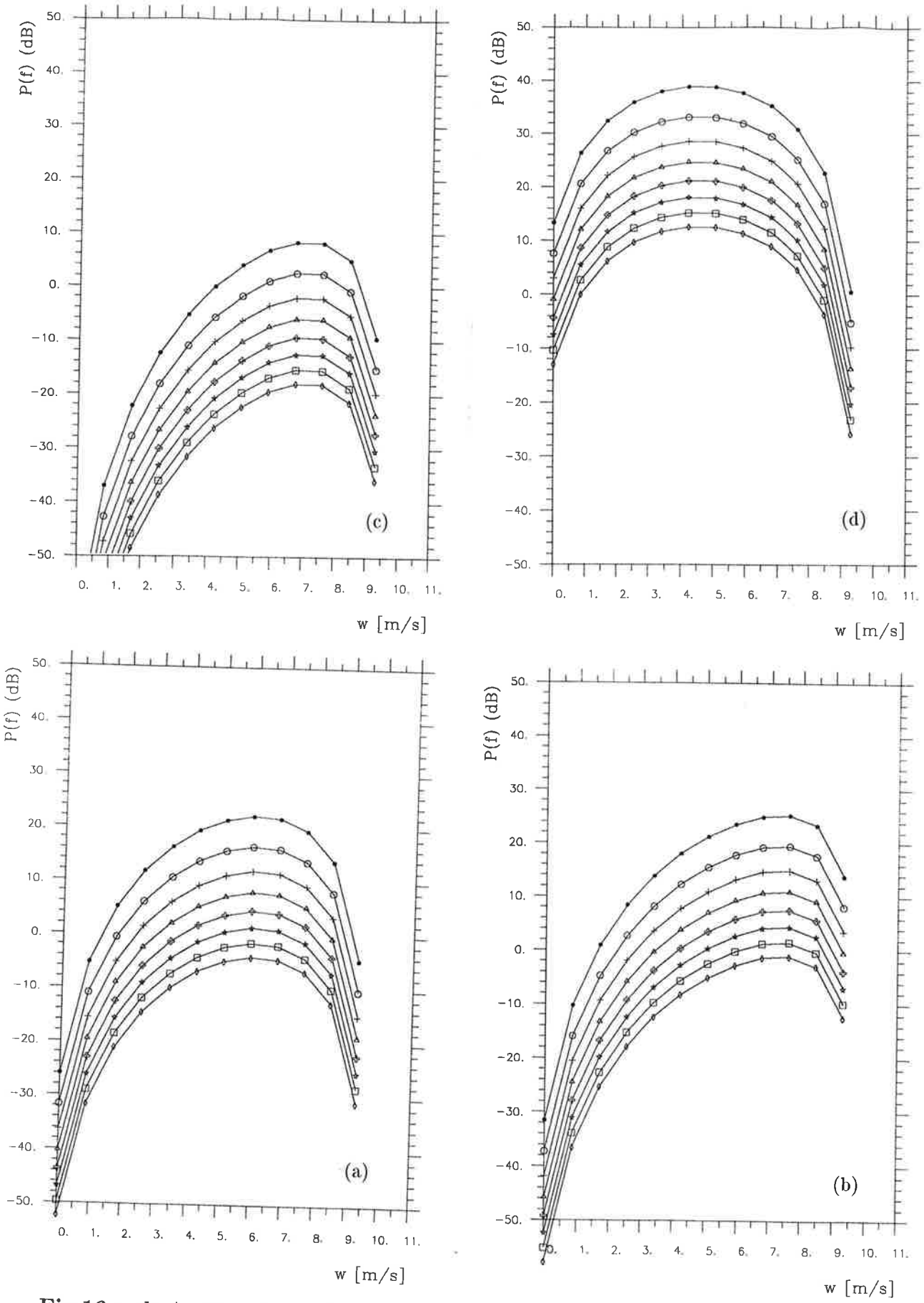

Fig.16 a-d: As Fig. 15 but for a 12.5 kHz sodar

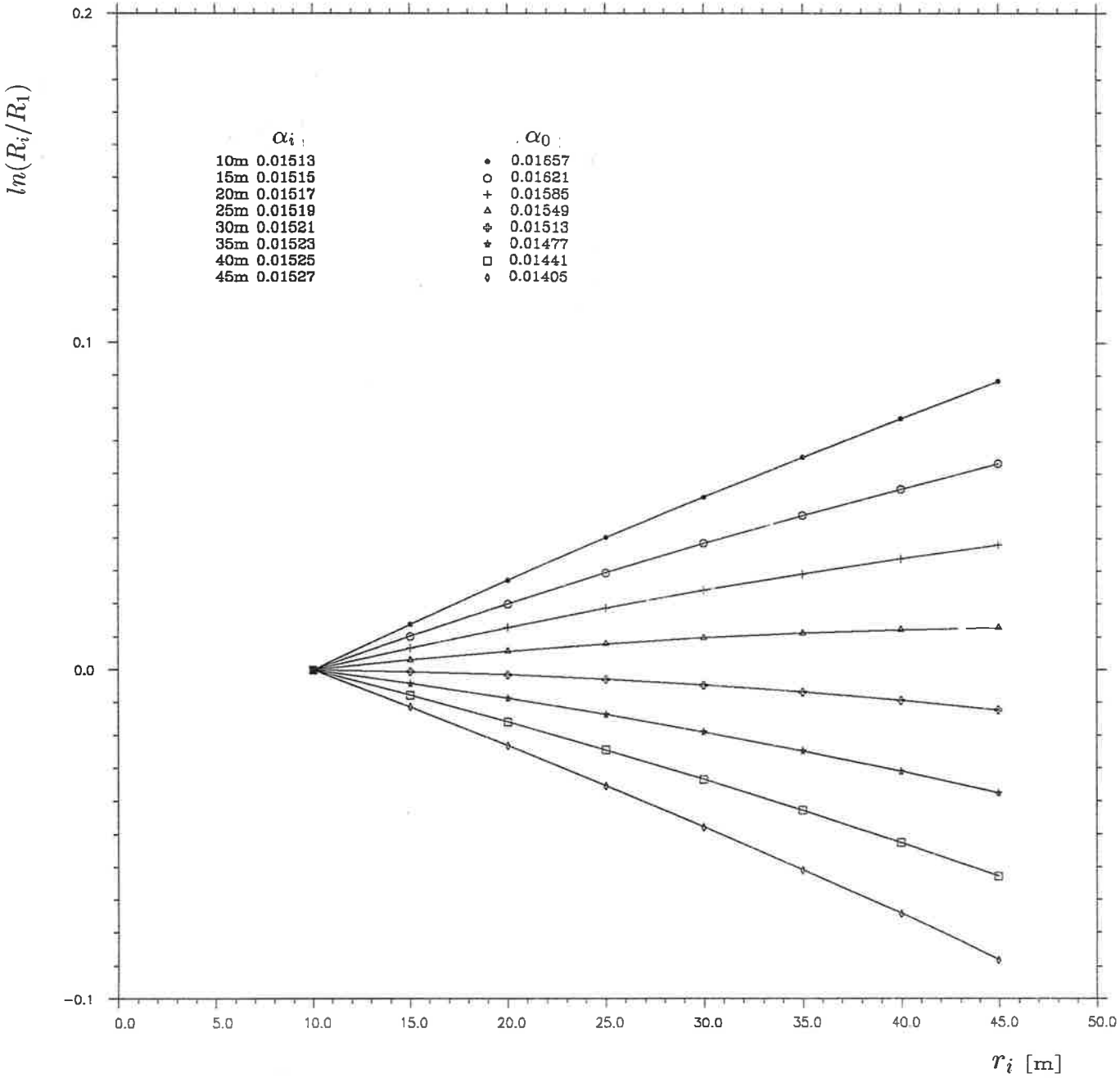

Fig.17 : Logarithm of rainrate ratio $Y_i = ln\frac{R_i}{R_1}$ versus r_i for a 6.4kHz sodar at different surface temperature, i.e. different α_0 listed in figure, which are used for first R_i retrieval. The simulation correspondes to a linear temperature disteribution from 2^oC at 10m to 1.79^oC at 45m for the case of relative humidity $RH = 95\%$.

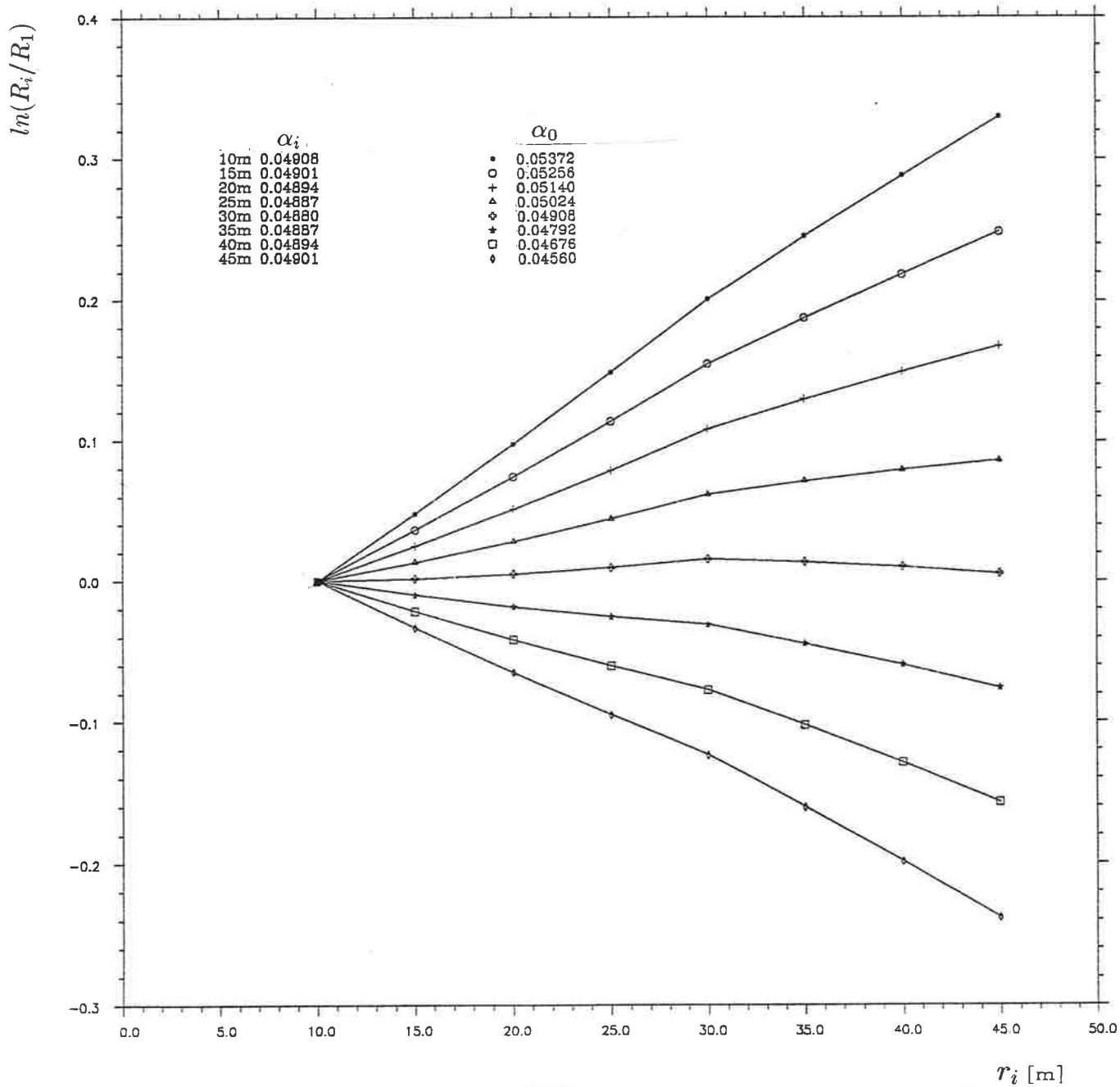

Fig.18 : As Fig.19 but for 12.5kHz and a corresponding temperature profile is from 2^oC at 10m linearly increasing to 2.12^oC at 30m but further decreasing to 2.03^oC at 45m.

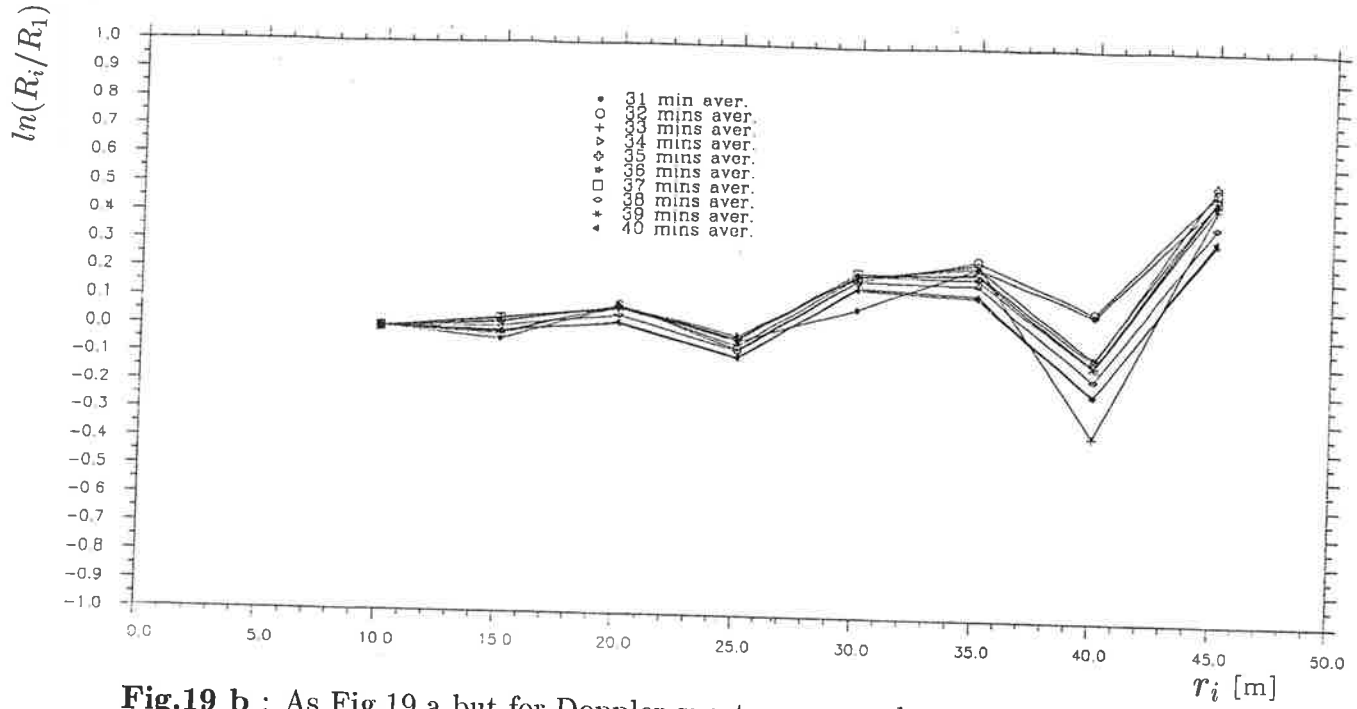

Fig.19 b : As Fig.19 a but for Doppler spectra averaged over 31 to 40 min

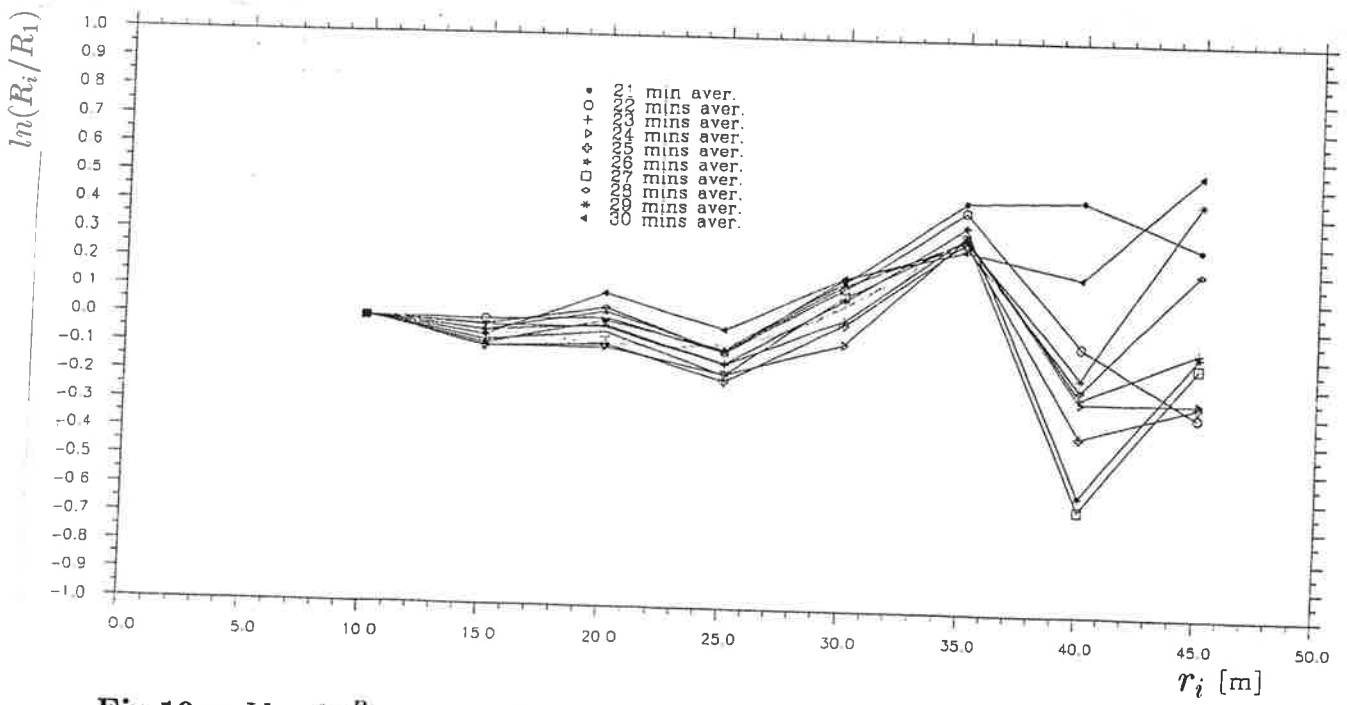

Fig.19 a: $Y_i = ln\frac{R_i}{R_1}$ versus r_i for measurements averaged over 21 min to 30min, starting time is 005502(UTC), 6 Jan 1993

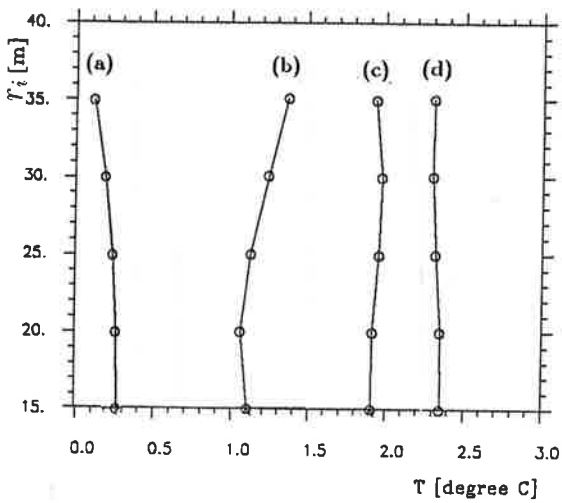

Figure 20: Temperature profiles retrieved from rainfall sodar Doppler spectra averaged over 30 min, starting time 192302(UTC) for (a), 213302 for (b) on 5 Jan 1993, 001502 (UTC) for (c) and 025502 for (d) on 6 Jan 1993.